Infrasound Radiation from Impulsive Volcanic Eruptions: Nonlinear Aeroacoustic 2D Simulations

Leighton M. Watson^{1,2}, Eric M. Dunham^{2,3}, Danyal Mohaddes⁴, Jeff Labahn⁵, Thomas Jaravel⁵, Matthias Ihme⁴

¹Department of Earth Sciences, University of Oregon, Eugene, Oregon, 97403, USA
 ²Department of Geophysics, Stanford University, Stanford, California, 94305, USA
 ³Institute of Computational and Mathematical Engineering, Stanford University, Stanford, California, 94305, USA

⁴Department of Mechanical Engineering, Stanford University, Stanford, California, 94305, USA
⁵Center for Turbulence Research, Stanford University, Stanford, California, 94305, USA

Key Points:

10

12

13

- Aeroacoustic simulations from the start-up of a pressure-balanced jet model fluid flow and infrasound radiation
- Compact monopole source model underpredicts the erupted volume for eruptions with sonic or supersonic exit velocities
- Infrasound radiation pattern depends on jet dynamics and is anisotropic for eruptions with sonic or supersonic exit velocities

Corresponding author: Leighton M. Watson, lwatson2@uoregon.edu

Abstract

18

19

20

22

23

24

25

26

27

28

30

31

32

33

34

35

38

30

40

41

42

43

45

46

47

49

50

53

54

55

Infrasound observations are commonly used to constrain properties of subaerial volcanic eruptions. In order to better interpret infrasound observations, however, there is a need to better understand the relationship between eruption properties and sound generation. Here we perform two-dimensional computational aeroacoustic simulations where we solve the compressible Navier-Stokes equations with a large-eddy simulation approximation. We simulate idealized impulsive volcanic eruptions where the exit velocity is specified and the eruption is pressure-balanced with the atmosphere. Our nonlinear simulation results are compared with the commonly used analytical linear acoustics model of a compact monopole source radiating acoustic waves isotropically in a half space. The monopole source model matches the simulations for low exit velocities ($M \lesssim 0.3$ where M is the Mach number); however, the two solutions diverge as the exit velocity increases with the simulations developing lower peak amplitude and more rapid onset. For high exit velocities (M > 0.8) the radiation pattern becomes anisotropic, with stronger infrasound signals recorded above the vent than on Earth's surface (50% greater peak amplitude for an eruption with M = 0.95) and interpreting ground-based infrasound observations with the monopole source model can result in an underestimation of the erupted volume. We examine nonlinear effects and show that nonlinear effects during propagation are relatively minor. Instead, the dominant nonlinear effect is sound generation by the complex flow structure that develops above the vent. This work demonstrates the need to consider anisotropic radiation patterns and near-vent fluid flow when interpreting infrasound observations, particularly for eruptions with sonic or supersonic exit velocities.

Plain Language Summary

Volcanic eruptions are noisy phenomena. During an eruption material is thrown into the atmosphere, pushing air out of the way and generating low frequency sound waves termed infrasound. We use infrasound observations to learn about the properties of volcanic eruptions. However, our understanding of the complex processes that generate sound during a volcanic eruption is limited. In order to address this, we perform simulations of volcanic eruptions and the associated infrasound signal. We compare our simulation results to an analytical model that is commonly used to interpret volcano infrasound observation. We show that for low exit velocities (M < 0.3 where M is the Mach number) the analytical model does a good job in explaining the infrasound observations and the radiation pattern. However, for higher exit velocities (M > 0.8) the analytical model overpredicts the peak amplitude of the infrasound signal, underpredicts the erupted volume, and does not account for the directionality of the radiation pattern. This work quantifies some of the complexities that should be considered when interpreting infrasound observations and is a step towards developing more sophisticated source models for volcanic eruptions.

1 Introduction

During a volcanic eruption material is ejected from the volcano into the atmosphere and the eruptive fluid interacts with the atmospheric air to form a jet. The displacement and compression of the atmospheric air by the expansion of the jet generates acoustic waves, which are predominantly at low frequencies and are termed infrasound (Johnson & Ripepe, 2011; Fee & Matoza, 2013). Infrasound observations are widely used to detect and monitor volcanic activity (Arnoult et al., 2010; Coombs et al., 2018; Ripepe et al., 2018; De Angelis et al., 2019) as well as to constrain eruption properties including eruptive volume and mass (Johnson & Miller, 2014; Kim et al., 2015; Fee et al., 2017; Iezzi et al., 2019), plume height (Caplan-Auerbach et al., 2010; Yamada et al., 2017), and crater dimensions (Fee et al., 2010; Richardson et al., 2014; Johnson et al., 2018; Witsil & Johnson, 2018; Watson et al., 2019, 2020).

The majority of volcano infrasound studies assume compact (i.e., point) sources, linear wave propagation, and do not account for fluid flow in the complex region near the vent. These simplifying assumptions have been extremely useful for interpreting volcano infrasound signals and relating observations to eruption properties (see De Angelis et al. (2019) for a review). However, in order to improve infrasound-derived constraints of eruption properties and leverage infrasound observations to learn more about eruptive processes and jet dynamics, we need to revisit these assumptions and consider more realistic source models.

Many volcano infrasound studies describe the acoustic source as a point monopole source in a homogeneous half-space (e.g., Vergniolle & Brandeis, 1996; Johnson & Miller, 2014; Yamada et al., 2017; De Angelis et al., 2019), which has an isotropic radiation pattern. It is challenging to measure the radiation pattern for a volcanic eruption because most infrasound sensors are deployed on Earth's surface. Several studies have utilized surrounding topography to improve the vertical coverage of infrasound sensors (Johnson et al., 2008; Rowell et al., 2014; McKee et al., 2017) while recent work suspended infrasound sensors from tethered aerostats and observed anisotropic radiation patterns (Jolly et al., 2017; Iezzi et al., 2019).

There are several possible explanations for the observed anisotropic radiation patterns. First, this might be caused by scattering of acoustic waves from complex volcanic topography (Kim & Lees, 2014; Kim et al., 2015; Fee et al., 2017). Second, several authors have argued for a dipole source mechanism for certain eruptions (Woulff & McGetchin, 1976; Johnson et al., 2008; Caplan-Auerbach et al., 2010), which produces an anisotropic radiation pattern. Third, a spatially distributed source can appropriately be described as compact or a point source when the source dimension is small compared to the characteristic wavelength ($ka \ll 1$ where a is the source dimension and k is the wavenumber with $k=2\pi/\lambda=2\pi f/c$ where λ is the wavelength, f is the frequency and c is the speed of sound). For many volcanic eruptions $ka \sim 1$ and finite source effects, which are when acoustic waves from different parts of the source arrive at the receiver at different times, can be important. Our simulations neglect topography but naturally capture finite source effects, possible dipole contributions and other fluid dynamic complexities that may be present in real eruptions.

Linear wave propagation is justified for sufficiently small pressure perturbations. In this limit, changes in sound speed from changes in temperature are negligible, and fluid particle velocities are small compared to the sound speed such that advection is also negligible. Volcanic eruptions, however, are violent phenomena that can generate large pressure amplitudes and large Mach number fluid motions, such that nonlinear propagation effects might be important.

In recent work, Anderson (2018) and Maher et al. (2020) performed nonlinear acoustic simulations of waves radiating from a region of initially high density or pressure. In

their simulations, the sound speed depends on the temperature but fluid flow and advection were not included. Anderson (2018) applied scaling analysis from the chemical/nuclear explosion literature to volcanic eruptions and showed how a single eruption simulation can be scaled for a range of eruption energies, which reduces computational expense. Maher et al. (2020) used a quadspectral density-based nonlinear indicator to detect and quantify wavefront steepening, which could be used to identify nonlinear propagation effects in field observations. In contrast to the work of Anderson (2018) and Maher et al. (2020), Brogi et al. (2018) performed nonlinear computational aeroacoustic simulations that include both acoustic waves and fluid flow, with the acoustic waves excited by fluid flow from a vent. They focused on short duration explosions and their simulations show an acoustic wave propagating away from the vent in all directions, trailed by a jet of eruptive fluid extending upwards from the vent. Brogi et al. (2018) showed that the radiation pattern became more anisotropic as the exit velocity was increased, with larger pressure amplitudes above the vent than to the side. Due to their use of a lattice Boltzmann numerical method, their simulations were limited to subsonic velocities (M < 0.5 where M is the Mach number).

The fluid dynamics during a volcanic eruption can be extremely complex. Near the vent, erupted material forms a momentum-driven jet, which is often referred to as the gas thrust region. As the erupted material rises, it can expand and form a plume by entraining and heating the surrounding atmospheric air. If sufficient entrainment occurs, the plume can become buoyant and continue to rise. Otherwise, the plume can collapse a form a pyroclastic density current (Sparks & Wilson, 1976; Neri & Macedonio, 1996; Clarke et al., 2002; Neri et al., 2003; Koyaguchi & Suzuki, 2018). There has been extensive modeling of plume (Wilson et al., 1978, 1980; M. I. Bursik & Woods, 1991; Ogden, Glatzmaier, & Wohletz, 2008) and jet dynamics (Woods, 1988; M. Bursik, 1989; Ogden, Wohletz, et al., 2008; Koyaguchi et al., 2010; Ogden, 2011; Suzuki & Koyaguchi, 2012; Koyaguchi et al., 2018). The majority of modeling work has used steady state vent conditions and studied the development and evolution of volcanic jets and plumes. Here, we consider unsteady vent conditions and focus on the volcanic jet.

The two dominant controls on jet dynamics are exit velocity and pressure at the vent. Ogden, Wohletz, et al. (2008) and Koyaguchi et al. (2018) examined the influence of vent pressure on steady jet dynamics. For over-pressurized vents (vent pressure greater than atmospheric pressure), their simulations show underexpanded jets with complex flow structures, including standing shock waves (Mach disks and barrel shocks) and the flow partitioning into an outer sheath that moves faster than the inner core. For pressure balanced jets, there are no standing shock waves or flow partitioning but vortex rings develop on either side of the jet. Suzuki and Koyaguchi (2012) examined the impact of exit velocity on jet dynamics for steady state vent conditions and suggest that the efficiency of entrainment decreases with increasing exit velocity, which hampers the development of the jet into a buoyant plume and can lead to collapse. Other factors that might impact jet dynamics are vent radius and geometry (Koyaguchi et al., 2010; Ogden, 2011) and the contrast in fluid properties between the eruptive fluid and the atmosphere, but for simplicity we do not examine these effects in our study.

Despite substantial work on volcano infrasound and jet dynamics, there are very few modeling studies linking jet dynamics with infrasound observations (e.g., Brogi et al., 2018). This is because it is computationally challenging to simulate acoustic waves along with fluid flow. Most CFD methods introduce artificial dissipation to handle shocks at the expense of overdamping acoustic waves (Lele, 1997).

Here, we build upon the existing jet dynamics (e.g., Ogden, Wohletz, et al., 2008; Suzuki & Koyaguchi, 2012; Koyaguchi et al., 2018) and volcano infrasound (e.g., Anderson, 2018; Brogi et al., 2018; Maher et al., 2020) literature by performing two-dimensional (2D) simulations of idealized short-duration volcanic eruptions and their associated infrasound radiation. Simulations are performed using the nonlinear computational aeroa-

coustics code, $\operatorname{CharLES}^X$ (Khalighi et al., 2011; Ma et al., 2018), which can simulate fluid flow and acoustic waves at the same time. We consider simplified eruptions of pressure-balanced jets (vent pressure equal to atmospheric pressure) where the eruptive fluid has the same composition as the atmospheric air. We explore the sensitivity of the infrasound signal to exit velocity, examine the radiation pattern, and compare our simulation results with the solution for a compact monopole source.

2 Acoustics

Many volcano infrasound studies describe the acoustic source as a point monopole in a homogeneous half-space and assume linear wave propagation (e.g., Vergniolle & Brandeis, 1996; Johnson & Miller, 2014; Yamada et al., 2017; De Angelis et al., 2019). For a monopole point source radiating in a 3D whole space, the pressure perturbation is given by (Lighthill, 1952)

$$\Delta p(R,t) = \frac{\rho_0}{4\pi R} \ddot{V}(t - R/c_0), \tag{1}$$

where Δp is the pressure perturbation, V is the volume and ρ_0 is the density of displaced atmospheric air, R is the distance from the source to receiver, and c_0 is the background speed of sound. In many volcano infrasound studies the volume of displaced atmospheric air, V, is assumed to be equal to the volume of erupted material (e.g., Fee et al., 2017).

In order to take into account the bounding effect of Earth's surface, equation 1 can be modified for radiation into a half space (Johnson et al., 2012; Johnson & Miller, 2014; Yamada et al., 2017; Watson et al., 2019):

$$\Delta p(R,t) = \frac{\rho_0}{2\pi R} \ddot{V}(t - R/c_0), \tag{2}$$

where the radiation angle is reduced from 4π to 2π . Equations 1 and 2 have an isotropic radiation pattern (same in all directions). Example infrasound signals generated by a monopole point source with a Gaussian volume rate in a half space are shown in Figure 1.

In this study, we perform computational aeroacoustic simulations in 2D for computational efficiency. A 2D model assumes invariance in one horizontal coordinate direction, which changes the monopole point source to a line source. In order to compare between our computational simulations and analytical models, we consider the monopole line source solution (analogous to the monopole point source solution of equation 2):

$$\Delta p(R,t) = \frac{\rho_0}{2\pi} \int_0^{t-R/c_0} \frac{\ddot{A}(\tau)}{\sqrt{(t-\tau)^2 - R^2/c_0^2}} d\tau, \tag{3}$$

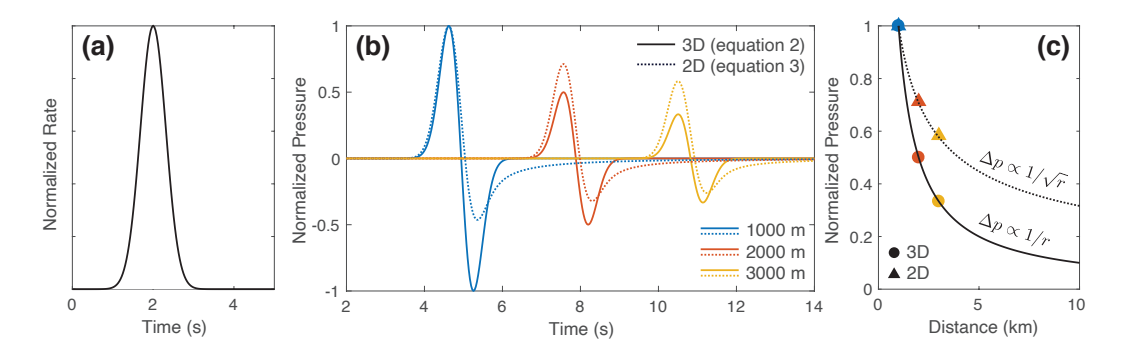


Figure 1. Example infrasound signal for a monopole point source (i.e., 3D, solid) and line source (i.e., 2D, dotted) in a half space. (a) Acoustic waves are excited by a Gaussian pulse, which is volume rate in 3D (m³/s) and area rate in 2D (m²/s). (b) Analytical infrasound signals at 1000 m (blue), 2000 m (red), and 3000 m (yellow) from the point source (solid) and line source (dotted) computed using equations 2 and 3, respectively, and the rate shown in (a). (c) Peak pressure as a function of distance for point (circle) and line (triangle) sources. Black lines show 1/r (solid) and $1\sqrt{r}$ (dotted) decay. The infrasound signals are normalized by the peak amplitude at 1000 m.

where A is the area of displaced atmospheric air. Note that acoustic waves behave differently in 2D than in 3D. The amplitude decays as $1/\sqrt{R}$ instead of 1/R and the waveform shape is different; the rarefaction has lower amplitude and longer duration, as shown in Figure 1.

If the source dimension is sufficiently large (ka > 1) then the acoustic source cannot be modeled as compact. In this limit, finite source effects, which are not incorporated in the previous equations, are important. Acoustic waves from different parts of the source region reach the receiver at different times, which can result in complex anisotropic radiation patterns. Previous work has modeled infrasound radiation from wide volcanic craters as a baffled piston (Johnson et al., 2018; Watson et al., 2019) where the pressure perturbation in the frequency domain is given by (Rossing & Fletcher, 2004):

$$\Delta p(R,\omega,\theta) = i\omega \exp(-ikR) \frac{\rho_0}{2R\pi a^2} \left[\frac{2J_1(ka\sin\theta)}{ka\sin\theta} \right] V(\omega), \tag{4}$$

where ω is the angular frequency, $k=\omega/c_0$ is the wavenumber, a is the radius of the piston, θ is the angle from the vertical axis to the receiver, and J_1 is a Bessel function of order one. The infrasound radiation pattern given by equation 4 is anisotropic because it depends on the angle from the vertical; the amplitude of the signal will be larger for receivers directly above the vent $(\theta=0^\circ)$ than receivers on Earth's surface $(\theta=90^\circ)$. Figure 2 plots the baffled piston solution, showing how the amplitude of the infrasound signal can vary with angle and how the degree of anisotropy depends on the dimensionless parameter, ka. If ka>1, then finite source effects are important and the radiation pattern will be anisotropic. However, if $ka\ll 1$, then the finite source effects are negligible and the baffled piston solution reduces to the monopole point source half-space solution (equation 2) that features an isotropic radiation pattern.

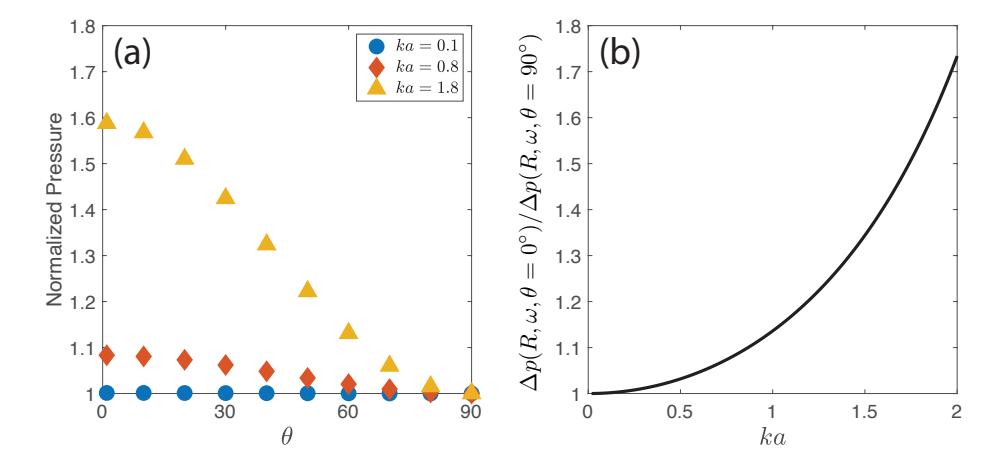


Figure 2. Baffled piston solution (Equation 4), which accounts for finite source effects. (a) Normalized peak pressure perturbation as a function of angle from the vertical, θ , for three different values of ka. As ka increases, the radiation pattern becomes more anisotropic with larger pressure signals measured above the vent ($\theta = 0^{\circ}$) than on Earth's surface ($\theta = 90^{\circ}$). (b) Ratio of peak pressure perturbation above the vent ($\theta = 0^{\circ}$) and on Earth's surface ($\theta = 90^{\circ}$). This provides a measure of the anisotropy of the signal (the signal more anisotropic when the ratio is larger) and shows that anisotropy increases as ka increases and finite source effects become important.

3 Computational Aeroacoustics and $CharLES^X$

In this section we describe the computational aeroacoustics code, $\operatorname{CharLES}^X$, that we use to perform our nonlinear simulations. $\operatorname{CharLES}^X$ is an aeroacoustics code that can simulate both fluid flow and acoustic waves, where the acoustic waves are generated naturally in the simulations by the compressible fluid dynamics. This differs from previous nonlinear infrasound studies by De Groot-Hedlin (2012), Anderson (2018), and Maher et al. (2020) in which acoustic waves are excited by a zone of initial high pressure or density and the complex fluid dynamics in the source region are not directly captured. Gravity is neglected due to our focus on jet dynamics rather than the plume.

CharLES^X is an unstructured mesh, finite-volume, large-eddy simulation (LES) code that is widely used in studies of jet noise and other aeroacoustics applications (Khalighi et al., 2011; Nichols et al., 2012; Hickey & Ihme, 2014; Brès et al., 2016; Ma et al., 2018; Chung et al., 2019; Jaravel et al., 2019; Lyrintzis & Coderoni, 2019; Ma et al., 2019). The code solves the filtered compressible Navier-Stokes equations in fully conservative form:

$$\partial_t \bar{\rho} + \nabla \cdot (\bar{\rho} \tilde{\boldsymbol{u}}) = 0, \tag{5a}$$

$$\partial_t \left(\bar{\rho} \tilde{\boldsymbol{u}} \right) + \nabla \cdot \left(\bar{\rho} \tilde{\boldsymbol{u}} \tilde{\boldsymbol{u}} \right) = -\nabla \bar{p} + \nabla \cdot \bar{\boldsymbol{\tau}}_{\nu+t}, \tag{5b}$$

$$\partial_t \left(\bar{\rho} \tilde{e}_t \right) + \nabla \cdot \left(\bar{\rho} \tilde{u} \tilde{e}_t \right) = -\nabla \cdot \left(\bar{p} \tilde{u} \right) + \nabla \cdot \left(\bar{\tau}_{\nu+t} \cdot \tilde{u} \right) - \nabla \cdot \bar{q}_{\nu+t}, \tag{5c}$$

where tilde and over-bar notations denote Favre and Reynolds filtering, respectively, which arise in the formal derivation of the LES equations for compressible flows (see Garnier et al. (2009) for details). Here, ρ is the density, \boldsymbol{u} is the velocity vector, p is the pressure, $\boldsymbol{\tau}_{\nu+t} = (\mu_{\nu} + \mu_t) \left(\nabla \tilde{\boldsymbol{u}} + (\nabla \tilde{\boldsymbol{u}})^T - \frac{2}{3}(\nabla \cdot \tilde{\boldsymbol{u}})\boldsymbol{I}\right)$ is the viscous stress tensor, \boldsymbol{I} is the identity matrix, $e_t = e_s + \frac{1}{2}\tilde{\boldsymbol{u}} \cdot \tilde{\boldsymbol{u}}$ is the specific total energy, $\boldsymbol{q}_{\nu+t} = -(\lambda_{\nu} + \lambda_t)\nabla T$ is the heat flux vector, and T is the temperature. Subscripts ν and t denote viscous and turbulent contributions, respectively. Sensible specific energy e_s , as well as molecular dynamic viscosity μ_{ν} and thermal conductivity λ_{ν} are obtained using the Cantera library (Goodwin et al., 2018) for thermodynamic, chemical kinetic, and transport processes although in this work we neglect any reactive chemistry effects.

Equations 5 are time-advanced using a third-order explicit Runge-Kutta time-stepping scheme (Hickey & Ihme, 2014; Ma et al., 2018). Spatial discretization is performed using a hybrid spatial differencing approach that switches between a low-dissipation centered (fourth-order accurate on uniform meshes) and a lower-order (either first-order or second-order essentially non-oscillatory, or ENO) scheme (Khalighi et al., 2011; Hickey & Ihme, 2014). The lower-order schemes are activated only in regions of high local density variation (e.g., shocks) using a threshold-based sensor (Hickey & Ihme, 2014). Boundary conditions are enforced using a penalty method in terms of characteristic variables (Poinsot & Lelef, 1992). When solving the Navier-Stokes equations, it is critical to account for the effects of the unresolved turbulence on the resolved flow using a sub-grid model (Khalighi et al., 2011). Sub-grid stresses are modeled using the Vreman (2004) eddy-viscosity model and a constant turbulent Prandtl number of 0.5.

CharLES^X can handle multiple, interacting fluids, which may be important to consider because the eruptive fluid generally has a different composition than the surrounding atmosphere. In this work, however, the erupted fluid has the same composition as the atmosphere, which allows us to focus on the influence of exit velocity. CharLES^X can also handle particle-laden flows (Mohaddes et al., 2021), with particles obeying their own Lagrangian equations of motion and having velocities that might differ from that of the gas. While this more rigorous treatment of ash particles has been shown to have important effects in conduit flow and jets (Dufek & Bergantz, 2007; Dufek et al., 2012; Benage et al., 2016), we defer these effects for future work.

4 Results

Here, we perform 2D computational aeroacoustic simulations of idealized impulsive volcanic eruptions using $\operatorname{CharLES}^X$. We focus on short-duration strombolian and vulcanian eruption styles because they occur frequently and there is a wealth of available data that can be used to inform and validate modeling efforts. These smaller eruptions are computationally simpler and more tractable to simulate yet exhibit many of the complex processes influencing infrasound generation and propagation (e.g., entrainment, shocks), with findings transferable to more hazardous sub-plinian/plinian eruptions. Our simulation results are compared with the compact monopole model and finite-difference linear acoustics simulations (hereafter referred to as linear simulations; Almquist & Dunham, 2020) to investigate and quantify deviations from linear acoustics and finite source effects.

4.1 Simulation Setup

The 2D computational domain is shown in Figure 3 and is invariant in the z direction (i.e., we simulate an infinite planar jet). The domain is discretized into rectangular elements with 2 m resolution at the vent and stretched horizontally to 10 m at the boundaries (mesh refinement tests show that this is sufficient resolution to resolve features of interest). The domain is initialized with stationary air with a composition of 23% oxygen and 77% nitrogen, which defines the specific gas constant and specific heat (Goodwin et al., 2018). The pressure is 101,325 Pa and the temperature is 300 K, which gives a speed of sound of 347 m/s.

The computational domain is bounded at the bottom by Earth's surface with a 60 m diameter vent in the center and by outflow boundaries on the other three sides. At the outflow boundaries, a constant pressure condition is applied ($p_{\rm out}=101,325$ Pa). This simple boundary condition causes small reflections when acoustic waves interact with the boundary. However, the boundaries are sufficiently far away that the simulations finish before the small reflections interact with the area of interest. Earth's surface is modeled as an adiabatic wall boundary. At the vent, the two components of velocity, pres-

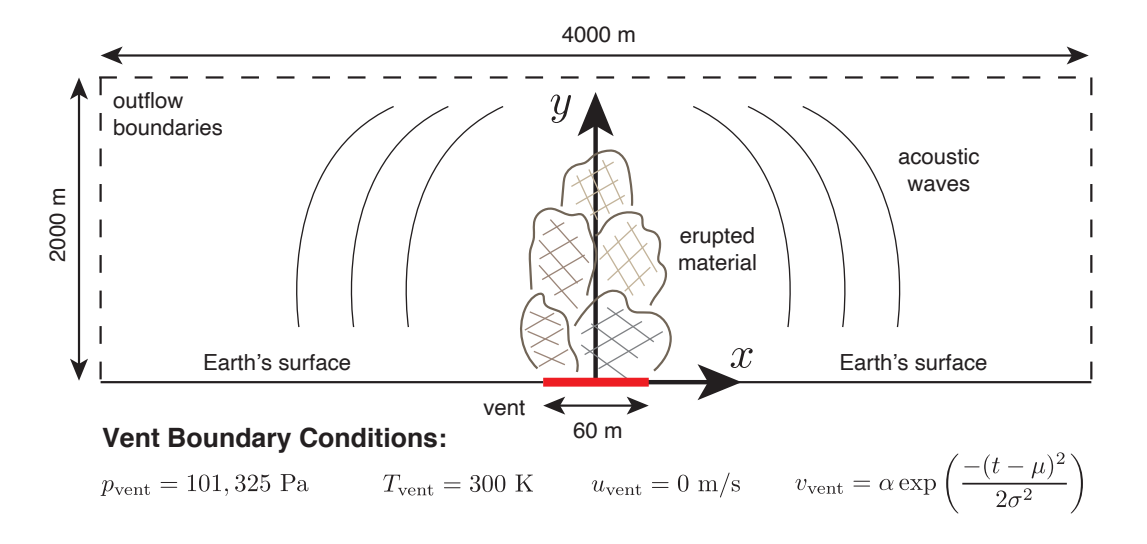
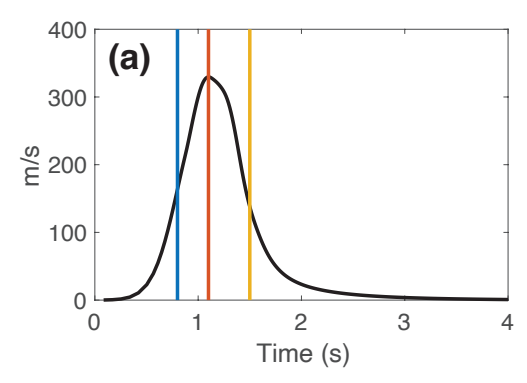


Figure 3. Schematic of two-dimensional computational domain. The bottom of the domain is divided into Earth's surface and the vent (red) where material is erupted. The four boundary conditions applied at the vent are shown below the schematic.



285

286

287

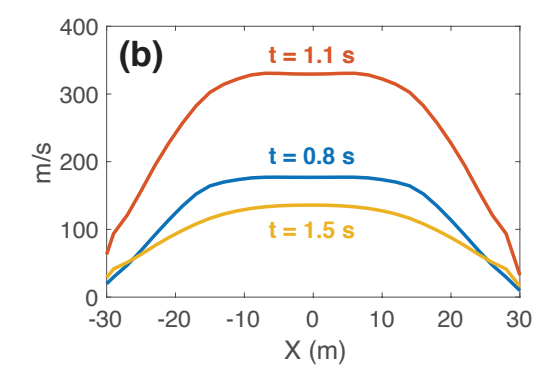


Figure 4. (a) Time series of vertical velocity at the center of the vent. (b) Vertical velocity profile across the vent at (blue) t = 0.8 s, (red) t = 1.1 s, and (yellow) t = 1.5 s. The vertical lines in (a) correspond to the times of the velocity profiles shown in (b).

sure, and temperature are specified. The horizontal velocity, u, is set equal to zero while the pressure and temperature are prescribed to be the same as the atmospheric conditions (101,325 Pa and 300 K, respectively). The vertical velocity, v, is prescribed as a Gaussian pulse:

$$v(t) = \alpha \exp\left(\frac{-(t-\mu)^2}{2\sigma^2}\right),\tag{6}$$

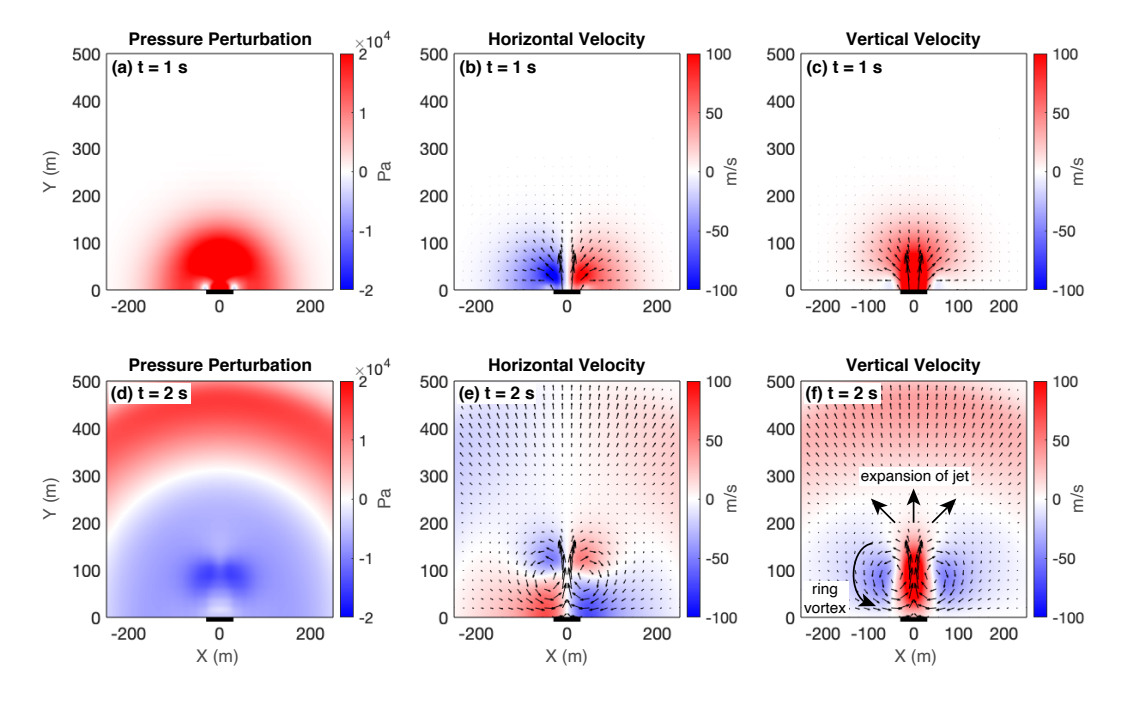


Figure 5. Snapshots of (a and d) pressure perturbation, (b and e) horizontal velocity, and (c and f) vertical velocity at (top) 1 s and (bottom) 2 s. The maximum exit velocity is 330 m/s and the vent location is indicated by the thick black line at the base of the plots. Velocity vectors are annotated on the horizontal and vertical velocity plots and show the development of vortex rings (Shariff & Leonard, 1992) on either side of the vent, as annotated in (f).

where v is the vertical velocity, α is the maximum amplitude, μ controls the center of the pulse and σ is determines the width. In this study we use $\mu = 1$ s, and $\sigma = 0.25$ s (an example vertical velocity time series is shown in Figure 4a). The vertical velocity varies spatially across the vent with a flat maximum in the center and tapering to zero at the edges of the vent (example vertical velocity profiles are shown in Figure 4b). For the Navier-Stokes equations, unlike the Euler equations, there is no difference in the number of boundary conditions specified for subsonic and supersonic inflows (Nordström & Svärd, 2005; Svärd et al., 2007). The boundary conditions are weakly enforced and therefore there can be some differences between the prescribed boundary condition and the simulation value. Time series of vertical velocity at the vent can have slightly lower amplitude and more extended decay that the prescribed Gaussian function and the pressure at the vent can deviate from atmospheric pressure. We define v_{max} as the maximum value of vertical velocity at the vent and note that due to the weak enforcement of the boundary conditions, $v_{\text{max}} < \alpha$. Due to the very small viscosity values, the no-slip condition on Earth's surface is effectively not enforced, as would be appropriate in the limit of the inviscid Euler equations.

4.2 Simulation Results

288

289

292

293

294

295

296

297

300

301

302

306

307

308

309

310

311

In this section, we present a detailed analysis of a single simulation for $v_{\text{max}} = 330 \text{ m/s}$ (M = 0.95). The vertical velocity at the center of the vent (x = 0) is shown in Figure 4a and several snapshots of the velocity profile across the vent are shown in Figure 4b. Snapshots of the pressure perturbation, horizontal and vertical velocity near the vent are shown in Figure 5. Figure 6 shows vertical profiles above the vent of pressure perturbation, vertical velocity, and speed of sound. Figure 7 shows horizontal profiles along the base of the domain of pressure perturbation, horizontal velocity, and speed of sound.

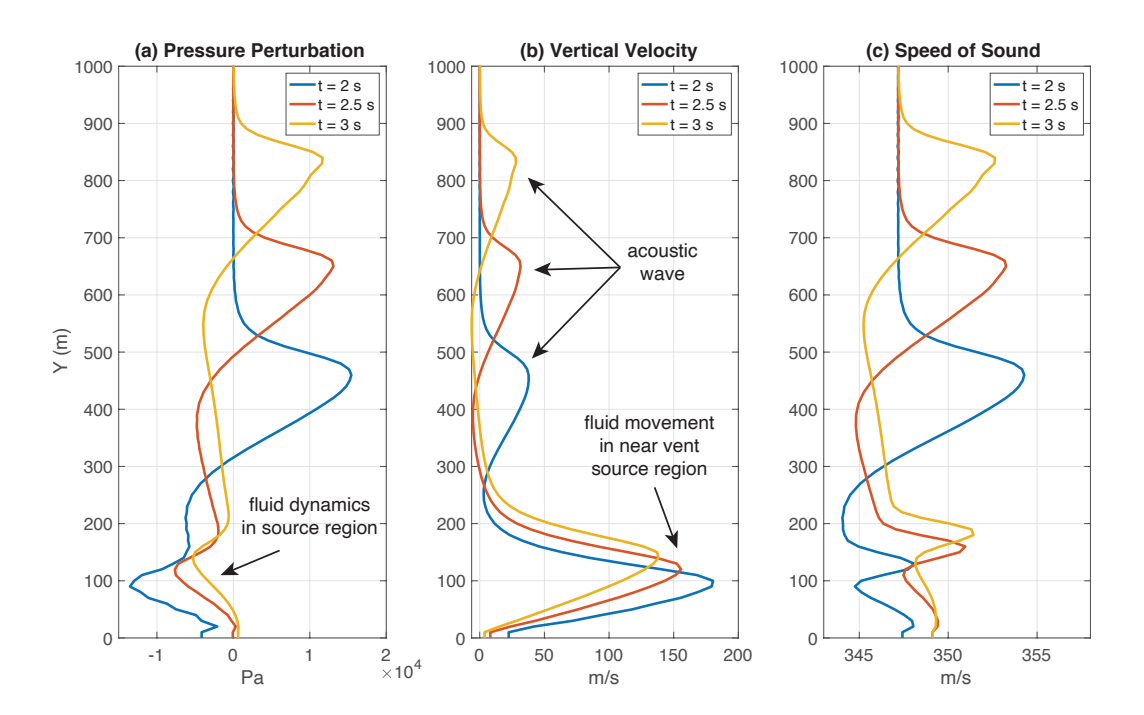


Figure 6. Vertical profiles of (left) pressure perturbation, (center) vertical velocity, and (right) speed of sound for a line of receivers above the vent (x = 0 m). Profiles are shown for three times: (blue) t = 2 s, (red) t = 2.5 s, and (yellow) t = 3 s.

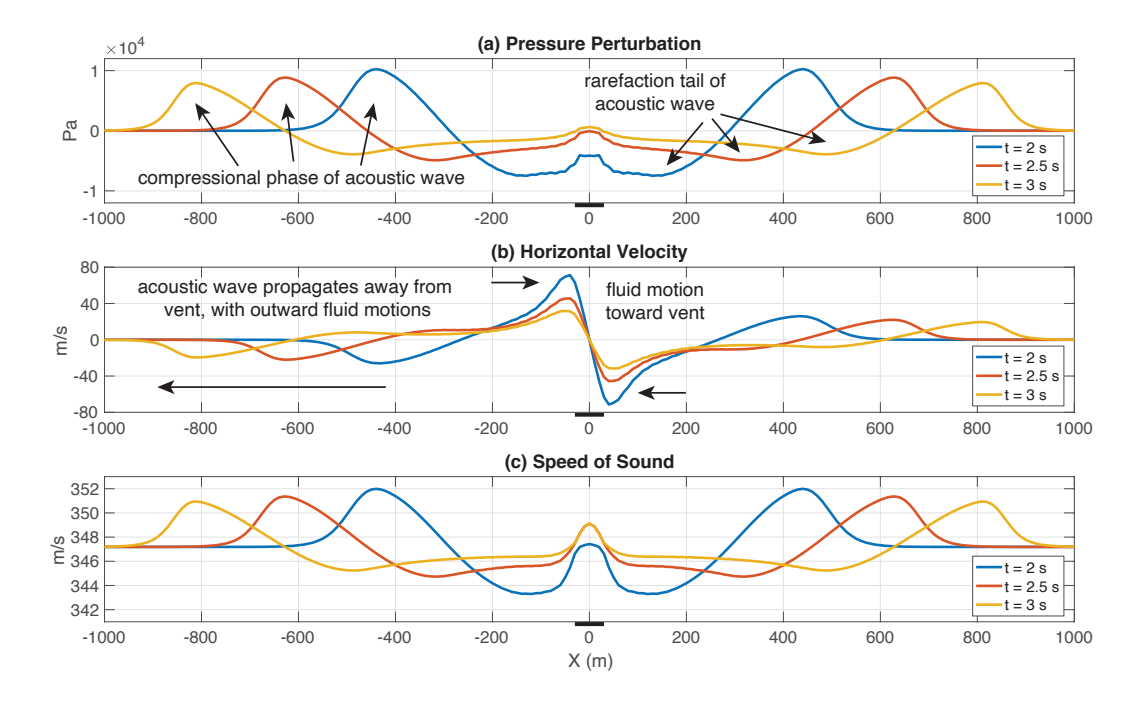


Figure 7. Horizontal profiles of (left) pressure perturbation, (center) horizontal velocity, and (right) speed of sound for a line of receivers along the base of the domain (y = 0 m). Profiles are shown for three times; (blue) t = 2 s, (red) t = 2.5 s, and (yellow) t = 3 s. The vent location is indicated by the black line at the base of the plots.

During the eruption, fluid is erupted out of the vent. This pushes on the atmosphere and generates an initial compressional pulse of pressure that propagates radially outwards from the vent. This is part of the acoustic pulse that is routinely observed in infrasound studies. As the pulse propagates further from the vent, a rarefaction tail, which is a well-known feature of 2D acoustics, develops (Figures 6a and 7a). The rarefaction is not clearly visible in the early time snapshots shown in Figure 5 because the acoustic pulse has not sufficiently separated from the fluid dynamics near the vent. In addition to the pressure pulse, the acoustic wave also causes particle motions radially away from the vent.

A jet of erupted material develops behind the acoustic wave at the eruption continues (Figure 5). The jet exhibits complex fluid dynamics and, for the pressure balanced vent conditions considered here, has a negative pressure perturbation. Directly above the vent, fluid rapidly moves vertically upwards. At the top part of the jet, the erupted fluid pushes outwards, forcing the atmospheric air into outward motion and causing the jet to expand with fluid moving horizontally away from the vent and vertically upwards. Outside of the vent, the fluid moves slowly downwards and fluid is recirculated horizontally back towards the vent at the base of the jet. This causes the formation of vortex rings (Shariff & Leonard, 1992) on either side of the vent (Figure 5e and 5f).

The acoustic waves steepen and the rarefaction tail becomes longer as the waves propagate farther from the vent (Figures 6a and 7a). Compression of the atmospheric air causes appreciable increases in temperature and consequently the local speed of sound. This causes the high pressure parts of the waveform to propagate faster, causing wavefront steepening and elongating the rarefaction tails (Hamilton & Blackstock, 2008). Anderson (2018) and Maher et al. (2020) have suggested this phenomena as the cause of asymmetric waveform recorded during volcano infrasound studies. For our simulations, however, the speed of sound changes shown in Figures 6c and 7c are relatively small ($\sim 2\%$) sug-

gesting that this is not the relevant nonlinearity. Instead, we contend that the nonlinear behavior is likely due to the nonlinear advection terms in the Navier-Stokes equations becoming significant as the fluid velocity approaches the speed of sound. More details about this are included in the Discussion section.

4.3 Exit Velocity

In this section, we examine the sensitivity of the infrasound signal to the exit velocity. We first examine the forward problem of calculating the infrasound signal from the eruptive rate and compare results of our nonlinear simulations to the linear acoustic monopole source model (equation 3). We then consider the inverse problem of inverting infrasound observations for the erupted volume rate and compare the inversion result with the true solution from our simulations.

4.3.1 Forward Problem

We perform simulations for a range of exit velocities between $v_{\text{max}} = 76 \text{ m/s}$ and $v_{\text{max}} = 588 \text{ m/s}$ and examine the infrasound signal recorded by probes along the Earth's surface. The simulations are compared with the compact monopole model (equation 3)

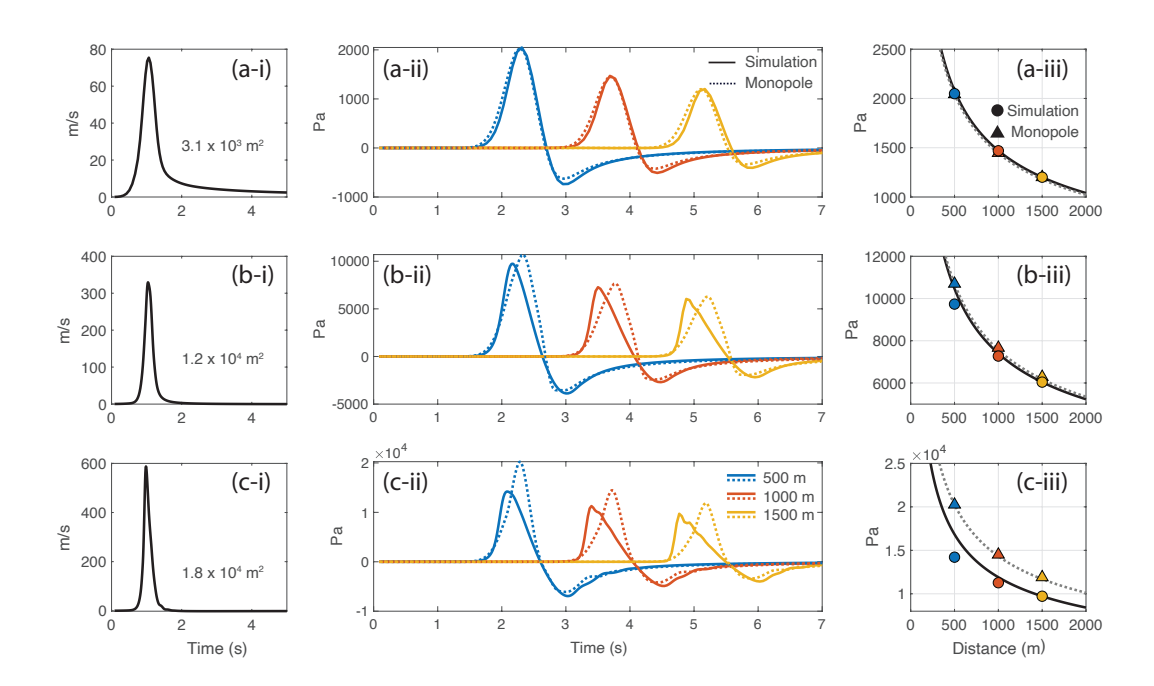


Figure 8. Comparison of infrasound signals from simulations (solid) and compact monopole model (dotted) for eruption sources with three different exit velocities: (a) $v_{\rm max} = 76$ m/s (M = 0.22), (b) $v_{\rm max} = 330$ m/s (M = 0.95), and (c) $v_{\rm max} = 588$ m/s (M = 1.69). (i) Exit velocity at center of vent. Numbers indicate the total erupted area. (ii) Infrasound time series recorded by probes at the base of the domain at three different distances from the center of the vent: (blue) 500 m, (red) 1000 m, and (yellow) 1500 m. (iii) Maximum pressure perturbation from the infrasound time series plotted as a function of distance for the simulations (circles) and the monopole model (triangles). The lines indicate the $1/\sqrt{r}$ decay of amplitude expected for linear propagation. The black solid line is fitted to the peak amplitude of the nonlinear simulations at 1500 m distance from the vent while the grey dotted line is fitted to the peak amplitude of the linear acoustics model at 1500 m from the vent.

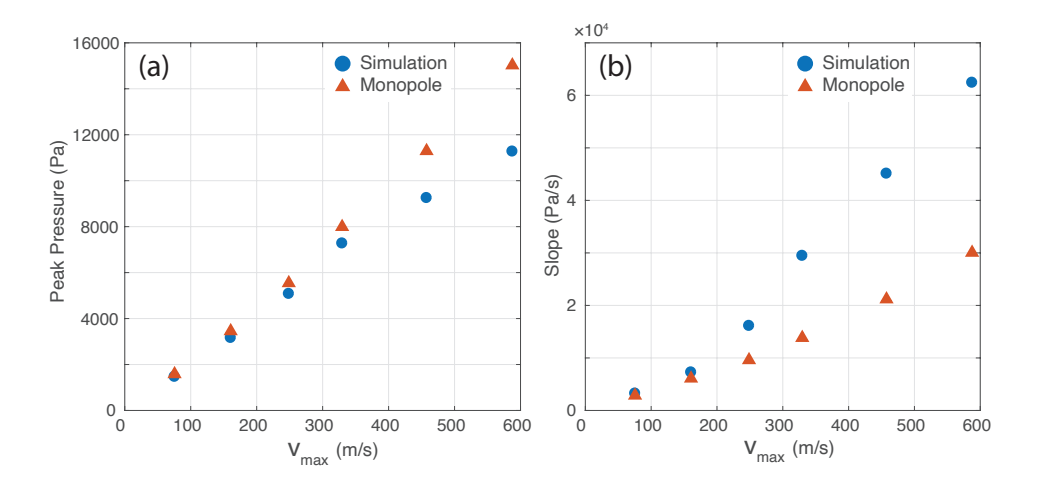


Figure 9. (a) Peak pressure and (b) slope of the infrasound signals from simulations (blue, circles) and the monopole model (red, triangles) as a function of maximum exit velocity. Infrasound signals are calculated at 1000 m from the vent. The slope is measured between 10% of the peak amplitude and the peak. The simulations and the monopole model are in agreement for low exit velocities (v_{max} < 200 m/s). However, when the exit velocity increases, the two solutions diverge with the simulations having a lower peak pressure and steeper slope.

where the area of the displaced atmospheric air is assumed to be equal to the area of erupted material (i.e., no entrainment).

A subset of the simulation results are shown in Figure 8. For low exit velocities ($v_{\rm max}$ =76 m/s; Figure 8a), the simulations and monopole model are in good agreement with similar arrival times, waveform shape, and peak amplitudes. The simulated infrasound signal decays in amplitude as $1/\sqrt{r}$, as expected from linear wave propagation theory, and the waveform does not change with distance from the vent. However, for high exit velocities ($v_{\rm max} > 330$ m/s; Figure 8b,c), the simulations diverge from the monopole model. The simulations have lower amplitude, faster onset, and slower amplitude decay than the monopole model. The simulated infrasound signals arrive sooner than for the monopole model, which suggests that advection may be important (advection is where the acoustic wave propagates at speed of sound plus the fluid velocity in the propagation direction). In addition, the waveform changes with distance from the vent. Figure 9 shows the peak pressure and slope as a function of exit velocity for the simulations and monopole model. This figure shows that the two solutions are in good agreement for low exit velocities but diverge as the exit velocity approaches and exceeds the speed of sound.

The simulation results presented here suggest that the compact monopole model, which assumes linear wave propagation, is an appropriate description for eruptions with low exit velocities. For high exit velocities, however, the monopole model is inappropriate and will result in an overestimation of the peak amplitude of the infrasound signal. We examine the sensitivity of the radiation pattern to exit velocity in Section 4.4 and discuss reasons for the differences between the simulations and monopole model in Section 5.

4.3.2 Inverse Problem

After examining the forward problem of calculating the infrasound signal for a given exit velocity, we now consider the inverse problem of estimating the erupted area from a given infrasound signal. We first simulate the infrasound signal for a range of exit ve-

locities. We then invert the simulated infrasound signal for the area rate, assuming a compact monopole source and linear wave propagation (equation 3). We assume that the area of displaced air is equal to the erupted area (i.e., no entrainment). The inverted area rate is compared with the true area rate, which is prescribed in the computational simulations. The goal of this section is to quantify how neglecting finite source effects and nonlinearities can bias estimates of the erupted volume (erupted area for our 2D simulations).

Equation 3 shows that the pressure perturbation in linear acoustics can be expressed as a convolution between the second time derivative of the area of displaced atmosphere, \ddot{A} , and a transfer function that describes the propagation, G:

$$\Delta p(r,t) = \ddot{A}(t) * G(r,t), \tag{7}$$

where * denotes the time-domain convolution. The convolution operation in the time domain corresponds to multiplication in the frequency domain:

$$\Delta \hat{p}(r,\omega) = \hat{A}(\omega)\hat{G}(r,\omega),\tag{8}$$

where ω is the angular frequency and $\hat{}$ denotes the Fourier transformed variable. The inversion problem can then be formulated as a time-domain deconvolution, which simplifies to division in the frequency domain:

$$\hat{A}(\omega) = \Delta \hat{p}(r,\omega) / \hat{G}(r,\omega). \tag{9}$$

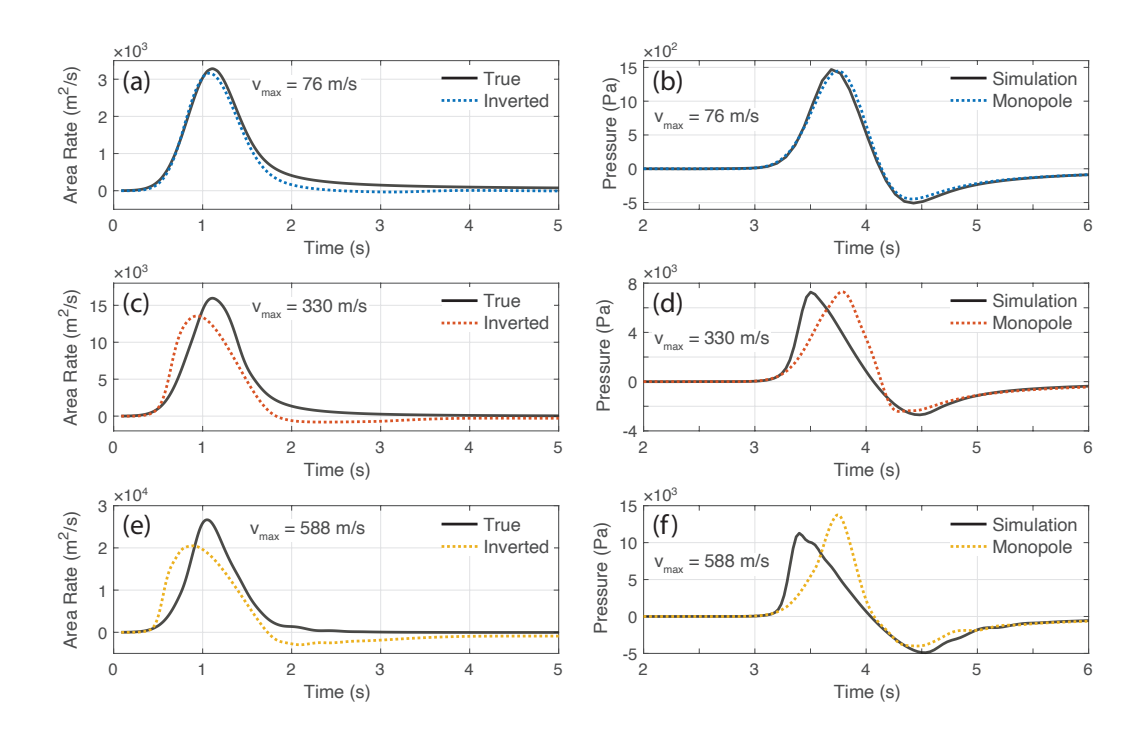


Figure 10. Comparison of true and inverted area rates for three different maximum exit velocities; (a and b) $v_{\rm max}=76$ m/s (M=0.22), (c and d) $v_{\rm max}=330$ m/s (M=0.95), and (e and f) $v_{\rm max}=588$ m/s (M=1.69). (a, c, and e) Area rate showing true (black, solid) and inverted (colored, dotted) values. Inverted values are calculated by inverting the pressure signals from the simulations (b, d, and f; black, solid) assuming compact monopole model (equation 3). (b, d, and f) Comparison of infrasound signals from simulations (black, solid) and from monopole model (colored, dashed) at 1000 m from the vent.

We then transform $\hat{A}(\omega)$ back to the time domain and integrate in time to obtain the area of the displaced atmospheric air, which we assume to be equal to the erupted area. The simulations are run for sufficient time so that the starting and ending pressure perturbations are zero (Johnson & Miller, 2014) and the inversions are performed for a single station.

Figure 10 the erupted area rate and associated infrasound signal for three exit velocities. For low exit velocities ($v_{\rm max}$ =76 m/s; Figure 10a,b) the inverted area rate is in good agreement with the true value. This is expected because the simulated and monopole infrasound signals are in good agreement. However, for high exit velocities ($v_{\rm max}$ >330 m/s; Figure 10c-f), the inverted area rate diverges from the true value. The inverted area rate has a faster rise to a lower peak value and more gradual decay to a negative value of area rate. We note that future work could utilize a more sophisticated inversion scheme where the area rate is constrained to be non-negative and multiple stations are used.

The area rate can be integrated to obtain the total erupted area. Figure 11 compares the true erupted area with the inverted erupted area. For low exit velocities ($v_{\text{max}} \lesssim 100 \text{ m/s}$), the true and inverted areas are in good agreement. For high exit velocities, however, the inverted area underpredicts the true value. For an exit velocity of 330 m/s, the inversion procedure underpredicts the erupted area by 30%. The error increases with increasing exit velocity and for an exit velocity of 588 m/s the inversion underpredicts the erupted area by 37%.

The results presented in this section show that interpreting volcano infrasound observations with a compact monopole model, which assumes linear wave propagation, can result in substantial underestimation of the erupted rate, especially when the exit velocity approaches or exceeds the speed of sound. In Section 5 we explore possible reasons for the discrepancy between our simulations and the monopole model. We consider nonlinear effects during propagation (temperature dependence of sound speed and advection), entrainment and complex fluid flow in the source region, and finite source effects. We note that we have so far only considered receivers along Earth's surface. In the next section we explore the infrasound radiation pattern and its dependence on exit velocity.

4.4 Radiation Pattern

The compact monopole model has an isotropic radiation pattern where acoustic energy is radiated equally in all directions. In this section, we examine the radiation pattern of our simulations and compare to the monopole model. As before, we consider three different maximum exit velocities in order to investigate the dependence of the radiation pattern on exit velocity. We examine the infrasound signal at 10 probes that are located between 0° and 90° from the jet axis at 10° intervals. The probes are all 1000 m radially from the center of the vent in order to measure the acoustic radiation that would be observed by infrasound sensors in the field rather than the fluid flow close to the vent, which from Figure 5 we see is confined to within ~ 200 m around the vent for the eruptions considered in this work.

For each simulation, we compute the sound pressure level and the peak pressure at each probe. The sound pressure level, measured in decibels, is commonly used in volcano infrasound and jet noise studies to describe acoustic signals (Matoza et al., 2007; Gee et al., 2008; Maher et al., 2020) and is defined as

$$SPL = 20\log_{10}\left(\frac{p_{\rm rms}}{p_{\rm ref}}\right),\tag{10}$$

where $p_{\rm rms}$ is the root mean square pressure and $p_{\rm ref}$ is the reference pressure of 20 $\mu {\rm Pa}$.

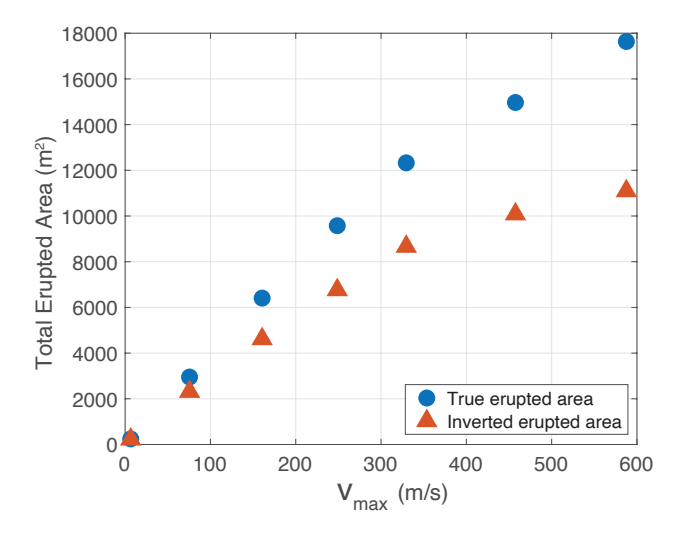


Figure 11. Total erupted area as a function of maximum exit velocity showing (blue, circles) true and (red, triangles) inverted erupted area. The inverted erupted area is calculated by inverting the nonlinear infrasound signals recorded at 1000 m from the vent using equation 3, which assumes linear wave propagation. The inverted area agrees with the true erupted area for low exit velocities, however, for sonic and supersonic exit velocities the inverted erupted area substantially underpredicts the true erupted area.

Figure 12 shows the change in sound pressure level and peak pressure as a function of angle from the jet axis in decibels and percentage, respectively. For $v_{\rm max}=76~{\rm m/s}$, the radiation pattern is relatively isotropic. The sound pressure level above the vent is only 0.29 dB greater than the value measured by a probe on the Earth's surface, which corresponds to a 7% increase in intensity. Similarly, the peak pressure perturbation above the vent is 6.6% larger than on Earth's surface. For high exit velocities, the radiation pattern becomes more strongly anisotropic. For $v_{\rm max}=330~{\rm m/s}$, the sound pressure

440

441

444

445

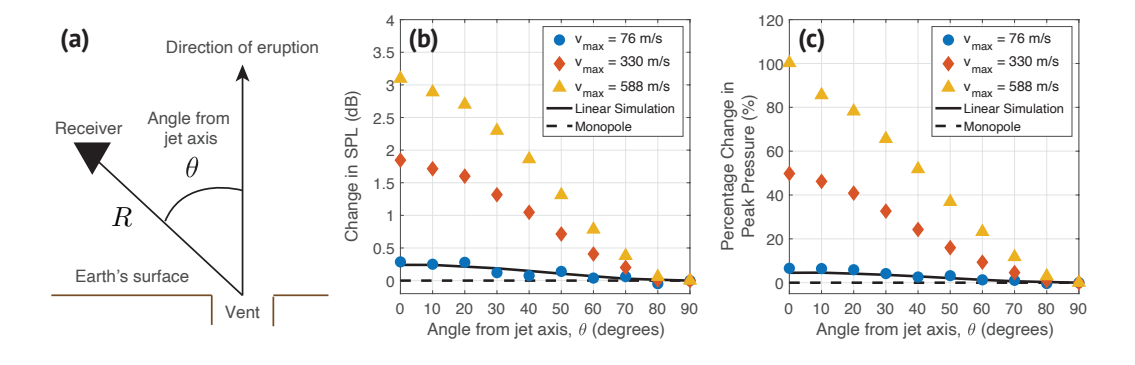


Figure 12. (a) Schematic showing probe location (R=1000 m) and angle from the jet axis, θ . (b) Change in sound pressure level as a function of θ . (c) Percent change in peak pressure as a function of θ . (b) and (c) show the radiation pattern from the nonlinear simulation for three exit velocities; (blue, circles) $v_{\text{max}} = 76 \text{ m/s}$, (M=0.22), (red, diamonds) $v_{\text{max}} = 330 \text{ m/s}$, (M=0.95), and (yellow, triangles) $v_{\text{max}} = 588 \text{ m/s}$, (M=1.69). The black solid line shows the linear simulation while the black dotted line shows the monopole solution.

level is 1.9 dB greater, corresponding to an intensity increase of 53%, when measured above the vent compared to on Earth's surface. For $v_{\rm max}=588$ m/s, the sound pressure level is 3.1 dB greater, corresponding to an intensity increase of 104%, when measured above the vent. Similarly, for maximum exit velocities of $v_{\rm max}=330$ m/s and $v_{\rm max}=588$ m/s, the peak pressure measured above the vent is 50% and 100% higher, respectively, compared to on Earth's surface.

There are several possible reasons for the anisotropic radiation pattern. First, the compact monopole model is only appropriate if $ka \ll 1$, as discussed in Section 2. For the simulations considered here, $ka \approx 0.3$ and therefore finite source effects may be significant. Second, material is erupted vertically upwards out of the vent and is relatively confined between thin shear layers on either side of the vent. This limits the horizontal expansion of the eruptive fluid and subsequent horizontal displacement of the atmospheric air. In contrast, the eruptive fluid expands rapidly in the vertical direction and hence atmospheric air may be preferentially displaced in the vertical direction. Third, the development of vortex rings causes atmospheric air to be pulled towards the vent at the base of the jet. The latter two possible reasons can be grouped together and referred to as complex fluid flow near the vent.

It is challenging to distinguish between finite source effects and fluid flow because both of these effects are included in our simulations but not in the compact monopole model. In order to disentangle these two effects, we perform linear acoustic simulations with the same geometry and boundary conditions as shown in Figure 3 using a finite-difference code (Almquist & Dunham, 2020), which we will refer to as the linear simulations. The linear simulations account for finite source effects but do not include fluid flow and hence allow these two effects to be distinguished.

For the linear simulations the radiation pattern is slightly anisotropic and independent of exit velocity. The sound pressure level recorded above the vent is 0.24 dB greater than on Earth's surface while the peak pressure is 4.5% greater, which are similar to the values for the $v_{\rm max}=76$ m/s simulation. This suggests that this small degree of anisotropy is due to finite source effects. For the higher exit velocities, however, the anisotropy is much more pronounced and cannot be explained by finite source effects. Instead, it is likely due to complex fluid flow near the vent, as we discuss further in Section 5.

5 Discussion

478

479

480

481

482

483

485

486

487

488

489

490

491

492

493

496

497

498

499

500

In this section, we explore possible reasons why the nonlinear computational simulations have different waveforms and radiation pattern to the monopole model. We discuss nonlinear propagation, finite source effects, and near-vent fluid dynamics.

5.1 Nonlinear Propagation Effects

For sonic and supersonic exit velocities, the simulated waveforms have steeper onset and more gradual decay than the monopole solution (Figure 8). Previous work has argued that these N-shaped waveforms can be caused by nonlinear propagation effects (e.g., Marchetti et al., 2013). Here, we investigate the significance of nonlinear propagation effects; the temperature dependence of the speed of sound and advection of acoustic waves.

The speed of sound is given by

$$c = \sqrt{\gamma QT},\tag{11}$$

where γ is the ratio of heat capacities, Q is the specific gas constant, and T is the temperature. Large amplitude pressure waves can compress the atmospheric air, causing adiabatic heating and hence increase the local sound speed. The high temperature parts of the waveform travel faster than the low temperature parts, which results in initially smooth waveforms steepening and forming shockwaves as energy is transferred to higher frequencies (Hamilton & Blackstock, 2008). The dependence of the local sound speed on temperature is a feature of nonlinear acoustics and is in contrast with linear acoustics where the speed of sound is assumed to be constant. We refer to this as the temperature nonlinearity. Anderson (2018) and Maher et al. (2020) invoked the temperature nonlinearity to explain asymmetric waveforms (waveforms with a steeper onset and more gradual decay than expected by linear theory) observed in their simulations.

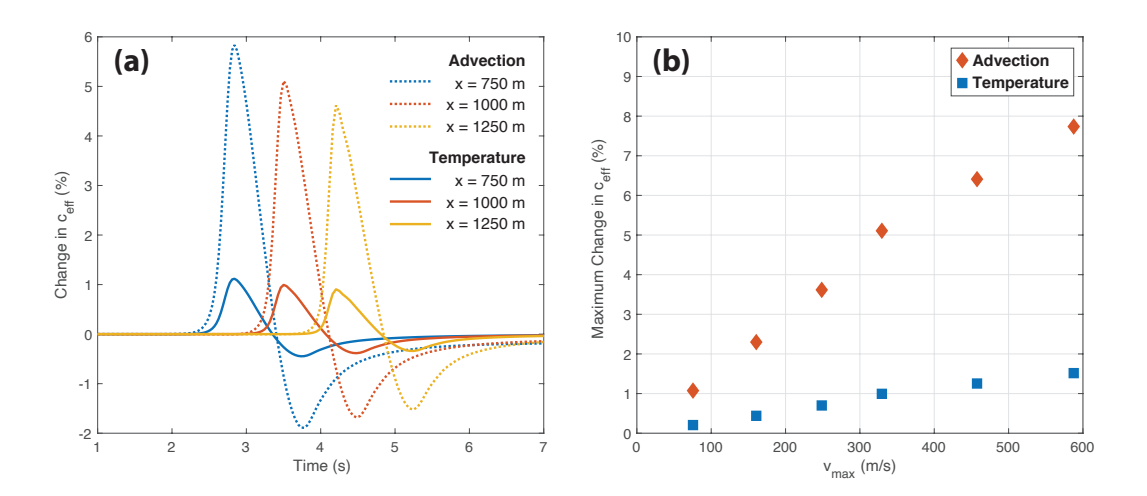


Figure 13. (a) Contribution of advection (equation 13; dotted) and temperature (equation 12; solid) nonlinearities to the effective sound speed as a function of time for three receiver positions along Earth's surface for an eruption with $v_{\text{max}} = 330 \text{ m/s}$; (blue) x = 750 m, (red) x = 1000 m, and (yellow) x = 1250 m. (b) Maximum contribution of advection (red, diamond) and temperature (blue, square) nonlinearities to the effective sound speed as a function of maximum exit velocity for a receiver along Earth's surface at x = 1000 m.

Another important nonlinear effect is advection, where waves propagate at the effective sound speed of $c_{\text{eff}} = \boldsymbol{v} \cdot \hat{\boldsymbol{n}} + c$ where \boldsymbol{v} is the velocity vector and $\hat{\boldsymbol{n}}$ is the normal vector in the direction of wave propagation. This is in contrast with linear acoustics where waves propagate at the background sound speed, c_0 , which is independent of fluid velocity. We refer to this as the advection nonlinearity.

501

502

503

505

506

507

510

511

513

514

515

516

517

518

519

522

523

526

527

530

531

532

533

534

535

538

539

540

541

544

545

546

We calculate the contributions of these two nonlinear propagation effects to the effective sound speed. The contribution of the temperature and advection nonlinearities are calculated as percentage changes from the background sound speed and are respectively given by:

temperature =
$$\frac{c - c_0}{c_0} \times 100$$
, (12)
advection = $\frac{\boldsymbol{v} \cdot \hat{\boldsymbol{n}}}{c_0} \times 100$.

$$advection = \frac{\boldsymbol{v} \cdot \hat{\boldsymbol{n}}}{c_0} \times 100. \tag{13}$$

Figure 13 shows a comparison of the two nonlinear effects. Figure 13a shows the relative contribution of the temperature and advection nonlinearities to the effective sound speed as a function of time for three receiver locations along Earth's surface for an eruption simulation with $v_{\text{max}} = 330 \text{ m/s}$. The station locations are chosen sufficiently far from the vent to focus on propagation effects and exclude nonlinearities from fluid flow near the vent, which are discussed in a later section. The temperature nonlinearity only causes a small change in the effective sound speed ($\sim 1\%$). This effect is relatively minor and unlikely to explain the wavefront steepening and shock formation as proposed by Anderson (2018) and Maher et al. (2020). The change in effective sound speed caused by the advection nonlinearity is approximately 5 times larger than that caused by the temperature nonlinearity. This shows that the advection is the dominant nonlinearity.

Figure 13b shows the maximum change in effective sound speed as a function of exit velocity for the temperature and advection nonlinearities. For both nonlinearities, the change in effective sound speed increases with increased exit velocity but the advection nonlinearity causes a much greater increase. This further demonstrates that, regardless of exit velocity, the advection nonlinearity is more significant than the temperature nonlinearity.

The work presented here shows that while the temperature nonlinearity does cause a small change in effective sound speed, the advection nonlinearity dominates. These simulations identify an important nonlinear phenomena that has not been previously discussed in the volcano infrasound literature. The nonlinear propagation effects discussed here can cause observed infrasound waveforms to differ from the waveforms predicted with a linear acoustics framework, such as the compact monopole model as shown in Figure 8. During a volcanic eruption, changes in fluid velocity during the passage of acoustic waves can change the speed of sound, which can lead to wavefront steepening and shock formation. These simulations show that asymmetric waveforms do not necessarily imply large changes in atmospheric temperature and can instead be caused by large fluid velocities, particularly caused by eruptions with high exit velocities. The changes in effective sound speed caused by nonlinear propagation effects, however, are relatively small (<10%) and in Section 5.3 we examine nonlinear effects in the source region.

5.2 Finite Source Effects

The nonlinear propagation effects discussed above can explain some of the differences between the simulated and monopole waveforms (Figure 8). Nonlinear propagation effects, however, are unable to explain the anisotropic radiation pattern observed in our simulations where the amplitude above the vent is greater than to the side (Figure 12). In this section we consider finite source effects as a possible explanation for the anisotropic radiation pattern.

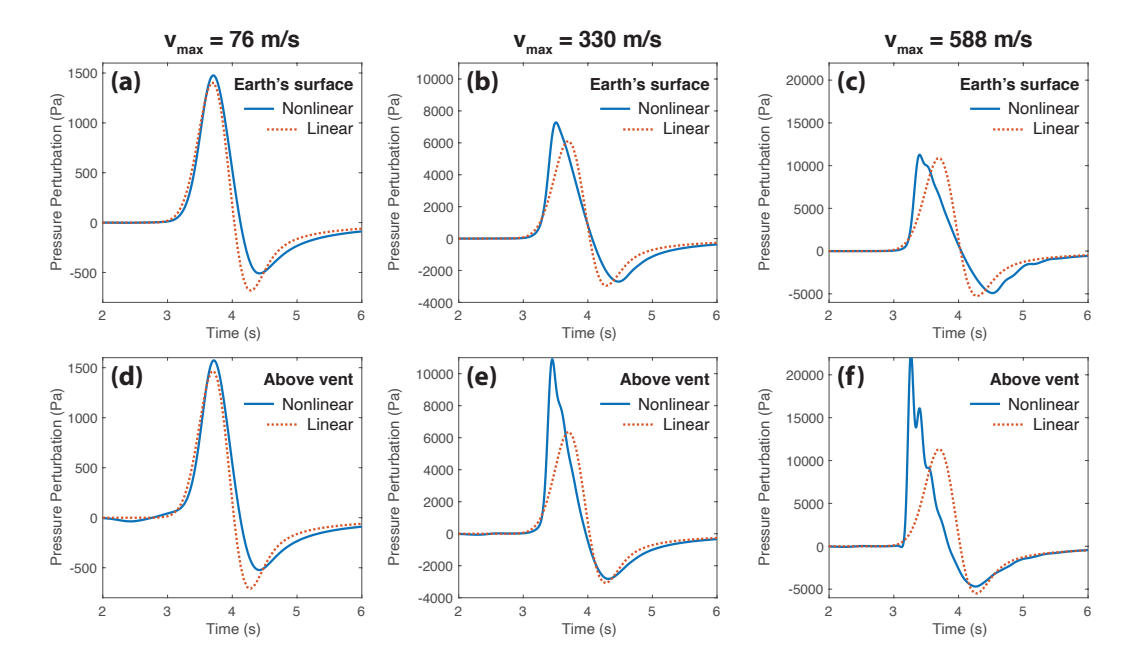


Figure 14. Infrasound waveforms for (blue, solid) nonlinear and (red, dotted) linear simulations for a receiver at (a, b, and c) 1000 m away from the vent on Earth's surface and (d, e, and f) 1000 m vertically above the vent. Three eruption simulations with different maximum exit velocities are shown; (a and d) $v_{\text{max}} = 76 \text{ m/s}$, (b and e) $v_{\text{max}} = 330 \text{ m/s}$, and (c and f) $v_{\text{max}} = 588 \text{ m/s}$.

Finite source effects can be important if the acoustic source is not spatially compact. For a compact source, the source dimension is small compared to the acoustic wavelength so that waves originating anywhere within the compact source region arrive at the receiver at effectively the same time. The radiation pattern for a compact monopole source is isotropic (equation 3 only depends on the source-receiver distance and not the receiver position). If the source dimension is large compared to the acoustic wavelength, however, then waves originating from different locations in the source region will arrive at the receiver at different times. This can result in an anisotropic radiation pattern, such as for a baffled piston (equation 4) where the pressure depends on the angle from the vertical axis as well as the source-receiver distance.

Infrasound waveforms for the nonlinear and linear simulations recorded above the vent and on Earth's surface are shown in Figure 14. For $v_{\rm max}=76$ m/s, the nonlinear and linear solutions are in reasonable agreement for a receiver on Earth's surface as well as above the vent. This demonstrates that the small amount of anisotropy present in the $v_{\rm max}=76$ m/s simulation (peak pressure amplitude is 4.5% larger above the vent than on Earth's surface) can be explained by finite source effects, which are accounted for in the linear simulation. This magnitude of anisotropy is in general agreement with the baffled piston solution that predicts the amplitude above the vent will be 10% larger than the amplitude on Earth's surface for ka=0.3, which is the approximate value for the simulations.

The nonlinear and linear simulations diverge as the exit velocity approaches and exceeds the speed of sound with the infrasound signals from the nonlinear simulations having steeper onset and larger amplitudes. The disagreement between the nonlinear and linear simulations is much more pronounced for receivers above the vent than on Earth's surface. For $v_{\rm max}=330$ m/s, the nonlinear simulation has a peak amplitude that is 17%

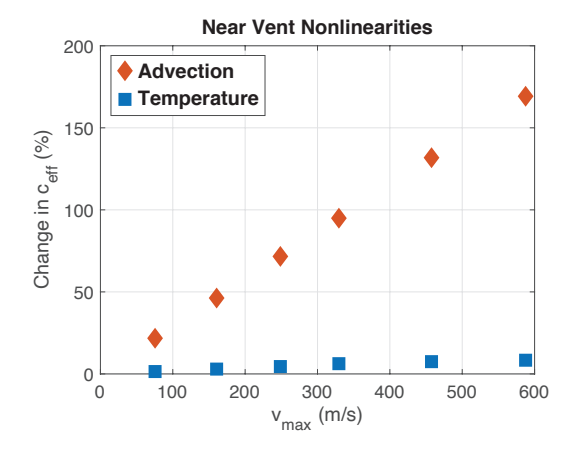


Figure 15. Maximum contribution of advection (red, diamond) and temperature (blue, square) nonlinearities as a function of maximum exit velocity for a receiver 10 m vertically above the center of the vent.

larger than the linear simulation for a receiver on Earth's surface but 83% larger for a receiver above the vent. This demonstrates that the large amount of anisotropy present in the $v_{\rm max}=330~{\rm m/s}$ and $v_{\rm max}=588~{\rm m/s}$ nonlinear simulations (peak pressure amplitude is 50% and 100% larger above the vent than on Earth's surface, respectively) cannot be explained by finite source effects and must be caused by physics that are not included in the linear simulations. In the next section, we discuss near-vent fluid flow as a possible explanation for the anisotropy that cannot be explained by finite source effects.

5.3 Near-Vent Fluid Dynamics

572

573

575

576

577

578

579

580

581

582

583

584

585

589

590

593

594

595

596

597

601

602

603

The fluid dynamics during a volcanic eruption can be extremely complex, particularly in the near-vent region where the pressure, temperature, and fluid velocity are at their highest values. Here, we investigate near-vent fluid dynamics as a possible explanation for (1) why the nonlinear simulations have larger amplitudes and steeper onsets than predicted by the monopole model for high exit velocities and (2) why the nonlinear simulations have much larger amplitudes above the vent than predicted by the monopole model or linear simulations for high exit velocities.

In Section 5.1, we considered the importance of the temperature and advection nonlinearities on the effective wave speed during propagation. We examined receivers at 1000 m from the vent in order to focus on propagation effects and concluded that while the advection nonlinearity dominated both effects were relatively minor during propagation (< 10% change in effective sound speed). Here we consider a receiver 10 m vertically above the center of the vent in order to examine nonlinear effects in the source region. Figure 15 shows the relative contribution of the temperature and advection nonlinearities in the source region and has the same trends as Figure 13b (advection nonlinearity is larger than temperature and both effects increase with increased exit velocity). However, the advection nonlinearity in the source region is an order of magnitude larger than the advection nonlinearity during propagation. Depending on the exit velocity, the advection nonlinearity in the source region can cause changes in the effective sound speed of up to 170%, which can cause wavefront steepening and shock formation. This suggests that nonlinear effects in the source region can cause substantial deviations in the waveform shape, amplitude, and arrival time from the predictions of the monopole model, such as shown in Figures 8 and 14. This result suggests that nonlinear effects may be more prevalent

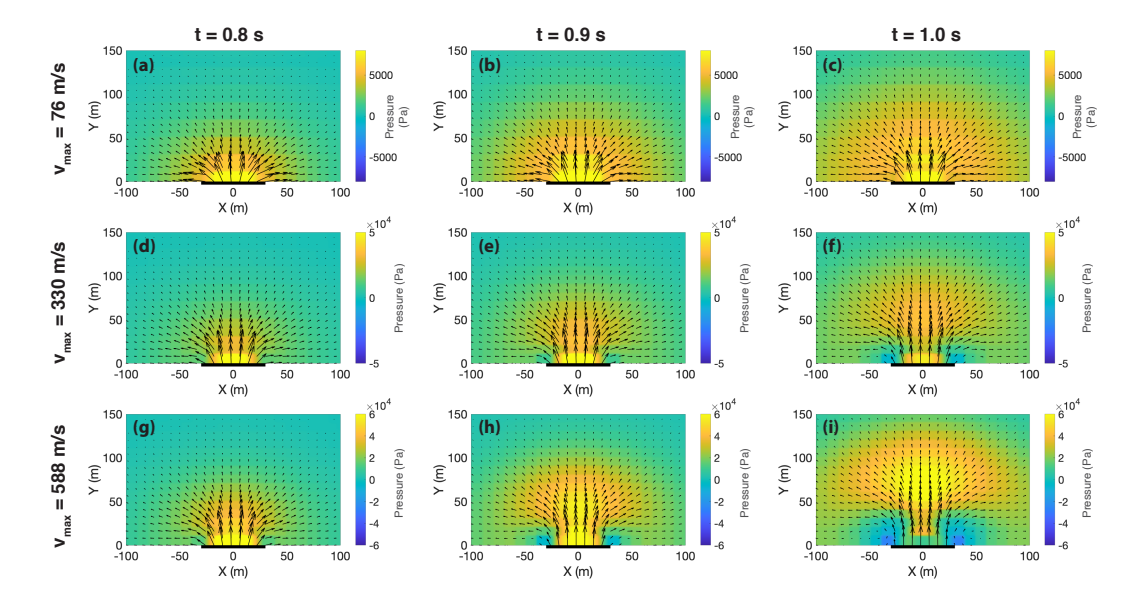


Figure 16. Fluid flow (black arrows) and pressure perturbation (colors) in the near-vent region at t = 0.8 s, t = 0.9 s, and t = 1.0 s for three simulations with different maximum exit velocities.

in volcanic eruptions than previously considered. It is much easier to achieve high temperatures and fast fluid velocities close to the vent than far away and hence, as shown in the simulations presented here, nonlinear effects are more likely to occur in the source than during propagation.

The nonlinear simulations have larger amplitudes above the vent than predicted by the monopole model or linear simulations. In Section 5.2 we showed that the small degree of anisotropy present for low exit velocities (peak amplitude of 4.5% larger above the vent than to the side for $v_{\rm max}=76~{\rm m/s}$) can be explained by finite source effects but the larger degree of anisotropy for the higher exit velocities cannot be (peak amplitude of 50% and 100% larger above the vent than to the side for $v_{\rm max}=330~{\rm m/s}$ and $v_{\rm max}=588~{\rm m/s}$, respectively). Here we consider near-vent fluid flow as a possible explanation. Figure 16 shows velocity vectors overlain on the pressure perturbation in the near-vent region for three simulations with different maximum exit velocities. The times are chosen to be around the source times for acoustic waves recorded at receivers 1000 m from the vent, as shown in Figures 12 and 14.

For $v_{\rm max}=76$ m/s, the erupted material expands in all directions and pushes the atmosphere outwards. This results in a radiation pattern that is approximately isotropic (apart from the small amount of anisotropy that was demonstrated in Section 5.2 to be due to finite source effects) and the simulated waveforms are in good agreement with the monopole model for both receivers on Earth's surface and above the vent. The good agreement between the simulated and monopole waveforms coupled with the similar radiation pattern suggests that in this instance the erupted volume is equal to the volume of displaced atmospheric air, which assumed in our application of the monopole model.

For $v_{\rm max}=330~{\rm m/s}$ and $v_{\rm max}=588~{\rm m/s}$, the erupted material preferentially expands upwards. Fluid is erupted vertically through the vent. Due to the sharp difference in velocity between the erupted fluid and the stationary atmospheric air, a thin shear layer is created on either side of the vent. This confines the eruptive fluid and inhibits expansion in the horizontal direction. High pressure develops above the vent and low pressure

sure on either side of the vent near Earth's surface. The low pressure on either side of the vent causes the recirculation of fluid back towards the vent, forming vortex rings on either side of the jet. The complex near-vent fluid dynamics shown in Figure 16 results in the infrasound signal recorded above the vent having larger amplitude than that recorded to the side of the vent on Earth's surface. The simulation results presented here demonstrate the near-vent fluid flow can have a significant impact on the observed infrasound signal, especially for eruptions with exit velocities approaching and exceeding the speed of sound where the fluid dynamics are more complex. Further work should continue to link infrasound observations with the complex fluid dynamics observed during volcanic eruptions.

5.4 Future Work

In this work, we perform 2D simulations of idealized volcanic eruptions. Our simulations contain several important simplifications and here we discuss how these simplifications may be addressed in future work.

In our simulations, the erupted material has the same composition and temperature as the atmosphere. For real volcanic eruptions, the erupted material can have a drastically different composition and temperature to the atmosphere as well as contain a significant fraction of solid particles. In particular, a more realistic eruptive fluid would have a much greater heat capacity and density but only slightly greater compressibility, due to rapid heat transfer from particles to the fluid that can buffer against adiabatic temperature changes. As the change in compressibility would be relatively small, the way that the eruptive fluid displaces and compresses the atmospheric air would likely be similar. The higher density of the erupted material, however, would result in greater inertia, which may further amplify the upward radiation relative to the side radiation. Therefore, the radiation pattern for a more realistic erupted fluid could be even more anisotropic than the simulation results presented here. CharLES X also has the capability to perform 3D simulations, incorporate variable fluid compositions, and simulate particle-laden flows (Mohaddes et al., 2021). These limitations can be addressed in future work to explore the impact of these phenomena on the infrasound signal.

Previous modeling work has examined overpressured jets (Ogden, Wohletz, et al., 2008; Ogden, Glatzmaier, & Wohletz, 2008; Koyaguchi et al., 2018). In this work, however, we focus on pressure-balanced jets, where the exit pressure is equal to atmospheric pressure. The jet dynamics in our simulations do not display the complex structures (barrel shocks, standing shocks, Mach disk) observed in overpressured jets (Ogden, Wohletz, et al., 2008; Koyaguchi et al., 2018). As such, this study should be viewed as the simplest possible case of jet dynamics and the associated infrasound signals. We defer a comprehensive study of the infrasound signals of overpressured jets for future work.

We focus on short-duration impulsive explosions that are representative of strombolian and vulcanian eruption styles. Previous work by Matoza et al. (2009) and Matoza et al. (2013) has focused on sustained jet noise, which is likely to occur during sub-plinian and plinian eruptions with sustained eruption columns. During these eruptions, sound is likely generated by turbulent structures within the jet (Matoza et al., 2013) rather than the bulk displacement of atmospheric air by the erupted material. There has been extensive work using $\operatorname{CharLES}^X$ to model noise from jet engines (Khalighi et al., 2011; Nichols et al., 2012; Brès et al., 2016) and future work could use $\operatorname{CharLES}^X$ to model sustained volcanic jetting during sub-plinian and plinian eruptions.

6 Conclusion

Volcanic eruptions frequently generate infrasound signals, however, the relationship between infrasound signals and eruption properties is not well understood. Volcanic eruptions are frequently approximated as monopole sources that radiate linear acoustic waves equally in all directions. There is growing appreciation that volcanic infrasound signals can be influenced by nonlinear propagation and finite source effects, exhibit anisotropic radiation patterns, and are sensitive to the complex fluid dynamics near the vent. In this study, we perform nonlinear computational aeroacoustic simulations of idealized short-duration impulsive volcanic eruptions in two-dimensions in order to better understand the relationship between infrasound observations and eruption properties.

We compare our nonlinear simulation results with the compact monopole source model. For low exit velocities ($v_{\rm max} < 100$ m/s or M < 0.3), infrasound observations are well described by the monopole model (assuming the source dimension is sufficiently small). As the exit velocity approaches and exceeds the speed of sound, however, the monopole model breaks down. The nonlinear infrasound observations are characterized by sharper onsets, more gradual decay, and lower peak amplitude than predicted by the monopole model. For $v_{\rm max} = 330$ m/s, the monopole source model underpredicts the slope measured by a receiver on Earth's surface by 53% and overpredicts the peak amplitude by 10%. Interpreting infrasound observations with the linear acoustics framework of the monopole source model can result in substantial underestimation of the erupted volume for eruptions with sonic and supersonic exit velocities (30% lower volume for an eruption with $v_{\rm max} = 330$ m/s and 37% for $v_{\rm max} = 588$ m/s).

The simulated infrasound radiation pattern is anisotropic with larger amplitudes recorded above the vent than to the side on Earth's surface. The degree of anisotropy scales with exit velocity; the peak pressure recorded at the vent is 4.5% larger than on Earth's surface for $v_{\rm max}=76~{\rm m/s}$ but 100% larger for $v_{\rm max}=588~{\rm m/s}$. This shows that for eruptions with high exit velocities, ground-based infrasound observations may substantially underpredict the acoustic power on an eruption. The large degree of anisotropy for the high exit velocity eruptions cannot be explained by finite source effects. Instead, it is due to complex fluid dynamics in the near-vent region. The formation of a shear layer on either side of the vent inhibits horizontal expansion and causes the erupted material to preferentially expand upwards, which results in greater pressure amplitudes above the vent than to the side.

Previous work has suggested that the temperature dependence of sound speed could causes wave front steepening and shock formation (Marchetti et al., 2013; Anderson, 2018; Maher et al., 2020). In our simulations, however, the effect of temperature nonlinearity effect is relatively minor. Instead, the advection term (waves travel at the background sound speed plus the local fluid velocity) is the dominant nonlinear propagation effect although this this effect only causes sound speed changes on the order of $\sim 10\%$. We are able to examine nonlinear effects in the source region and show that the advection nonlinearity can causes changes in the sound speed of up to $\sim 170\%$. This demonstrates that nonlinear source effects are much more significant than propagation effects and future work should focus on improving volcano infrasound source models.

Future work is needed to extend the simulations to 3D, to consider more realistic eruptive compositions and particle concentrations, and to explore the effect of vent overpressure. Nonetheless, this work highlights nonlinear propagation effects, finite source effects, and near-vent fluid flow as important factors to consider when interpreting volcano infrasound observations, especially for eruptions with sonic and supersonic exit velocities. In particular, we demonstrate that near-vent fluid dynamics are extremely important for infrasound generation. Future work should further explore the relationship between the complex near-vent fluid dynamics that are observed during volcanic activity and infrasound observations.

Acknowledgments

The simulation data and analysis code for this work are hosted at the Open Science Framework (doi:10.17605/OSF.IO/2EHUY). We thank the Center for Turbulence Research for providing us with academic access to the CharLES^X modeling code. We thank Robert Clapp for invaluable assistance with installing and running CharLES^X and Martin Almquist for helping with the linear acoustic simulations. This work was supported by National Science Foundation grants EAR-1930979 and EAR-1949219 and benefited from access to the high-performance computing resources provided by Stanford University's Center for Computational Earth and Environmental Sciences.

References

- Almquist, M., & Dunham, E. M. (2020). Non-stiff boundary and interface penalties for narrow-stencil finite difference approximations of the Laplacian on curvilinear multiblock grids. *Journal of Computational Physics*, 408, 109294. Retrieved from https://doi.org/10.1016/j.jcp.2020.109294 doi: 10.1016/j.jcp.2020.109294
 - Anderson, J. F. (2018). Pressure waves and tephra dispersal from volcanic explosions: models, observations, and instrumentation (Doctoral dissertation, Boise State University). doi: 10.18122/td/1468/boisestate
 - Arnoult, K. M., Olson, J. V., Szuberla, C. A. L., McNutt, S. R., Garcés, M. A., Fee, D., & Hedlin, M. A. H. (2010). Infrasound observations of the 2008 explosive eruptions of Okmok and Kasatochi volcanoes, Alaska. *Journal of Geophysical Research: Atmospheres*, 115, 1–12. doi: 10.1029/2010JD013987
 - Benage, M. C., Dufek, J., & Mothes, P. A. (2016). Quantifying entrainment in pyroclastic density currents from the Tungurahua eruption, Ecuador: Integrating field proxies with numerical simulations. Geophysical Research Letters, 43(13).
 - Brès, G. A., Jaunet, V., Le Rallic, M., Jordan, P., Towne, A., Schmidt, O. T., ... Lele, S. K. (2016). Large eddy simulation for jet noise: azimuthal decomposition and intermittency of the radiated sound. In *Aiaa/ceas aeroacoustics conference* (pp. 1–16). doi: 10.2514/6.2016-3050
 - Brogi, F., Ripepe, M., & Bonadonna, C. (2018). Lattice Boltzmann modeling to explain volcano acoustic source. Scientific Reports(May), 1–8. doi: 10.1038/s41598-018-27387-0
 - Bursik, M. (1989, 5). Effects of the drag force on the rise height of particles in the gas-thrust region of volcanic eruption columns. Geophysical Research Letters, 16(5), 441–444. Retrieved from http://doi.wiley.com/10.1029/GL016i005p00441 doi: 10.1029/GL016i005p00441
 - Bursik, M. I., & Woods, A. W. (1991). Buoyant, superbuoyant and collapsing eruption columns. *Journal of Volcanology and Geothermal Research*, 45, 347–350.
 - Caplan-Auerbach, J., Bellesiles, A., & Fernandes, J. K. (2010). Estimates of eruption velocity and plume height from infrasonic recordings of the 2006 eruption of Augustine Volcano, Alaska. *Journal of Volcanology and Geothermal Research*, 189(1-2), 12–18. doi: 10.1016/j.jvolgeores.2009.10.002
 - Chung, W. T., Ma., P. A., & Ihme, M. (2019). Examination of diesel spray combustion in supercritical ambient fluid using large-eddy simulations. *International Journal of Engine Research*, 1–12. doi: 10.1177/1468087419868388
 - Clarke, A. B., Voight, B., Neri, A., & Macedonio, G. (2002). Transient dynamics of vulcanian explosions and column collapse. *Nature*, 415 (July 1980), 897–901. doi: 10.1038/415897a
 - Coombs, M. L., Wech, A. G., Haney, M. M., Lyons, J. J., Schneider, D. J.,
 Schwaiger, H. F., ... Tepp, G. (2018). Short-Term Forecasting and Detection of Explosions During the 2016–2017 Eruption of Bogoslof Volcano, Alaska.
 Frontiers in Earth Science, 6. doi: 10.3389/feart.2018.00122
 - De Angelis, S., Diaz-Moreno, A., Zuccarello, L., De Angelis, S., Diaz-Moreno, A., & Zuccarello, L. (2019). Recent Developments and Applications of Acoustic Infrasound to Monitor Volcanic Emissions. *Remote Sensing*, 11(11), 1302. doi: 10.3390/rs11111302
 - De Groot-Hedlin, C. D. (2012). Nonlinear synthesis of infrasound propagation through an inhomogeneous, absorbing atmosphere. *Journal of Acoustical Society of America*, 132. doi: 10.1121/1.4731468
- Dufek, J., & Bergantz, G. W. (2007). Suspended load and bed-load transport of particle-laden gravity currents: The role of particle-bed interaction. *Theoretical* and Computational Fluid Dynamics, 21(2), 119–145. doi: 10.1007/s00162-007 -0041-6

Dufek, J., Manga, M., & Patel, A. (2012). Granular disruption during explosive volcanic eruptions. *Nature Geoscience*, 5(8), 561–564. doi: 10.1038/ngeo1524

- Fee, D., Garcés, M., Patrick, M., Chouet, B., Dawson, P., & Swanson, D. (2010). Infrasonic harmonic tremor and degassing bursts from Halema'uma'u Crater, Kilauea Volcano, Hawaii. *Journal of Geophysical Research*, 115(B11), B11316. doi: 10.1029/2010JB007642
- Fee, D., Izbekov, P., Kim, K., Yokoo, A., Lopez, T., Prata, F., ... Iguchi, M. (2017). Eruption mass estimation using infrasound waveform inversion and ash and gas measurements: Evaluation at Sakurajima Volcano, Japan. *Earth and Planetary Science Letters*, 480, 42–52. doi: 10.1016/J.EPSL.2017.09.043
- Fee, D., & Matoza, R. S. (2013). An overview of volcano infrasound: from hawaiian to plinian, local to global. *Journal of Volcanology and Geothermal Research*, 123–137. doi: 10.1016/j.jvolgeores2012.09.002
- Garnier, E., Adams, N., & Sagaut, P. (2009). Large eddy simulation for compressible flows. Springer.
- Gee, K. L., Sparrow, V. W., James, M. M., Downing, J. M., Hobbs, C. M., Gabrielson, T. B., & Atchley, A. A. (2008). The role of nonlinear effects in the propagation of noise from high-power jet aircraft. *Journal of the Acoustical Society of America*, 123, 4082. doi: 10.1121/1.2903871
- Goodwin, D., Speth, R., Moffat, H., & Weber, B. (2018). Cantera: An object-oriented software toolkit for chemical kinetics, thermodynamics, and transport processes. Retrieved from https://www.cantera.org/doi: 10.5281/zenodo.1174508
- Hamilton, M. F., & Blackstock, D. T. (2008). *Nonlinear acoustics*. Melville, New York: Academic Press.
- Hickey, J.-P., & Ihme, M. (2014). Large Eddy Simulation of Supercritical Mixing and Combustion for Rocket Applications. 52nd Aerospace Sciences Meeting(January), 1–13. doi: 10.2514/6.2014-0138
- Iezzi, A. M., Fee, D., Kim, K., Jolly, A. D., & Matoza, R. S. (2019). Three-Dimensional Acoustic Multipole Waveform Inversion at Yasur Volcano, Vanuatu. Journal of Geophysical Research: Solid Earth, 2018JB017073. doi: 10.1029/2018JB017073
- Jaravel, T., Labahn, J., Sforzo, B., Seitzman, J., & Ihme, M. (2019). Numerical study of the ignition behavior of a post-discharge kernel in a turbulent stratified crossflow. *Proceedings of the Combustion Institute*, 37, 5065–5072. doi: 10.1016/j.proci.2018.06.226
- Johnson, J. B., Anderson, J., Marcillo, O., & Arrowsmith, S. (2012). Probing local wind and temperature structure using infrasound from Volcan Villarrica (Chile). *Journal of Geophysical Research*, 117. doi: 10.1029/2012JD017694
- Johnson, J. B., Aster, R., Jones, K. R., & McIntosh, B. (2008). Acoustic source characterization of impulsive Strombolian eruptions from the Mount Erebus lava lake. *Journal of Volcanology and Geothermal Research*, 177(3), 673–686. doi: 10.1016/J.JVOLGEORES.2008.06.028
- Johnson, J. B., & Miller, A. J. C. (2014). Application of the Monopole Source to Quantify Explosive Flux during Vulcanian Explosions at Sakurajima Volcano (Japan). Seismological Research Letters, 85(6), 1163–1176. doi: 10.1785/0220140058
- Johnson, J. B., & Ripepe, M. (2011). Volcano infrasound: A review. *Journal of Volcanology and Geothermal Research*, 206(3-4), 61–69. doi: 10.1016/j.jvolgeores .2011.06.006
- Johnson, J. B., Watson, L. M., Palma, J. L., Dunham, E. M., & Anderson, J. F. (2018). Forecasting the eruption of an open-vent volcano using resonant infrasound tones. Geophysical Research Letters, 1–8. doi: 10.1002/2017GL076506
 - Jolly, A. D., Matoza, R. S., Fee, D., Kennedy, B. M., Iezzi, A. M., Fitzgerald, R. H., ... Johnson, R. (2017). Capturing the Acoustic Radiation Pattern of Strom-

bolian Eruptions using Infrasound Sensors Aboard a Tethered Aerostat, Yasur Volcano, Vanuatu. Geophysical Research Letters, 44 (19), 9672–9680. doi: 10.1002/2017GL074971

- Khalighi, Y., Ham, F., Nichols, J., Lele, S., & Moin, P. (2011). Unstructured Large Eddy Simulation for Prediction of Noise Issued from Turbulent Jets in Various Configurations. 17th AIAA/CEAS Aeroacoustics Conference (32nd AIAA Aeroacoustics Conference)(June), 5–8. doi: 10.2514/6.2011-2886
- Kim, K., Fee, D., Yokoo, A., & Lees, J. M. (2015). Acoustic source inversion to estimate volume flux from volcanic explosions. Geophysical Research Letters, 42(13), 5243–5249. doi: 10.1002/2015GL064466
- Kim, K., & Lees, J. M. (2014). Local Volcano Infrasound and Source Localization Investigated by 3D Simulation. Seismological Research Letters, 85(6), 1177–1186. doi: 10.1785/0220140029
- Koyaguchi, T., & Suzuki, Y. J. (2018). The Condition of Eruption Column Collapse: 1. A Reference Model Based on Analytical Solutions. *Journal of Geophysical Research: Solid Earth*, 123(9), 7461–7482. doi: 10.1029/2017JB015308
- Koyaguchi, T., Suzuki, Y. J., & Kozono, T. (2010). Effects of the crater on eruption column dynamics. *Journal of Geophysical Research*, 115(B7), B07205. doi: 10.1029/2009JB007146
- Koyaguchi, T., Suzuki, Y. J., Takeda, K., & Inagawa, S. (2018). The Condition of Eruption Column Collapse: 2. Three-Dimensional Numerical Simulations of Eruption Column Dynamics. *Journal of Geophysical Research: Solid Earth*, 123(9), 7483–7508. doi: 10.1029/2017JB015259
- Lele, S. K. (1997). Computational aeroacoustics A review. AIAA Meeting Papers on Disc(January), 1–15. doi: doi:10.2514/6.1997-18
- Lighthill, M. J. (1952). On sound generated aerodynamically: I. General theory. *Proc. Roy. Soc. London Ser. A*, 211, 564–587.
- Lyrintzis, A. S., & Coderoni, M. (2019). The use of large eddy simulations in jet aeroacoustics. In *Aiaa scitech 2019 forum*. American Institute of Aeronautics and Astronautics Inc, AIAA. doi: 10.2514/6.2019-0633
- Ma, P. C., Wu, H., Jaravel, T., Bravo, L., & Ihme, M. (2018). Large-eddy simulations of transcritical injection and auto-ignition using diffuse-interface method and finite-rate chemistry. *Proceedings of the Combustion Institute*, 000, 1–8. doi: 10.1016/j.proci.2018.05.063
- Ma, P. C., Wu, H., Labahn, J. W., Jaravel, T., & Ihme, M. (2019). Analysis of transient blow-out dynamics in a swirl-stabilized combustor using large-eddy simulations. *Proceedings of the Combustion Institute*, 37, 5073–5082. doi: 10.1016/j.proci.2018.06.066
- Maher, S. P., Matoza, R. S., Groot-Hedlin, C. D., Gee, K. L., Fee, D., & Yokoo, A. (2020). Investigating Spectral Distortion of Local Volcano Infrasound by Nonlinear Propagation at Sakurajima Volcano, Japan. *Journal of Geophysical Research: Solid Earth.* doi: 10.1029/2019JB018284
- Marchetti, E., Ripepe, M., Delle Donne, D., Genco, R., Finizola, A., & Garaebiti, E. (2013). Blast waves from violent explosive activity at Yasur Volcano, Vanuatu. Geophysical Research Letters, 40(22), 5838-5843. doi: 10.1002/2013 GL057900
- Matoza, R. S., Fee, D., Garcés, M. A., Seiner, J. M., Ramón, P. A., & Hedlin, M. A. (2009). Infrasonic jet noise from volcanic eruptions. *Geophysical Research Letters*, 36(8). doi: 10.1029/2008GL036486
- Matoza, R. S., Fee, D., Neilsen, T. B., Gee, K. L., & Ogden, D. E. (2013).

 Aeroacoustics of volcanic jets: Acoustic power estimation and jet velocity dependence. *J. Geophys. Res. Solid Earth*, 118, 6269–6284. doi: 10.1002/2013JB010303
 - Matoza, R. S., Hedlin, M. A., & Garcés, M. A. (2007). An infrasound array study of Mount St. Helens. *Journal of Volcanology and Geothermal Research*, 160(3-4),

249–262. doi: 10.1016/j.jvolgeores.2006.10.006

- McKee, K., Fee, D., Yokoo, A., Matoza, R. S., & Kim, K. (2017). Analysis of gas jetting and fumarole acoustics at Aso Volcano, Japan. *Journal of Volcanology and Geothermal Research*, 340, 16–29. doi: 10.1016/J.JVOLGEORES.2017.03.029
- Mohaddes, D., Xie, W., & Ihme, M. (2021). Analysis of low-temperature chemistry in a turbulent swirling spray flame near lean blow-out. *Proceedings of the Combustion Institute*, 38.
- Neri, A., Esposti Ongaro, T., Macedonio, G., & Gidaspow, D. (2003). Multiparticle simulation of collapsing volcanic columns and pyroclastic flow. *Journal of Geophysical Research: Solid Earth*, 108(B4), 2202. Retrieved from http://dx.doi.org/10.1029/2001JB000508 doi: 10.1029/2001JB000508
- Neri, A., & Macedonio, G. (1996, 4). Numerical simulation of collapsing volcanic columns with particles of two sizes. Journal of Geophysical Research: Solid Earth, 101(B4), 8153-8174. Retrieved from http://doi.wiley.com/10.1029/95JB03451 doi: 10.1029/95JB03451
- Nichols, J. W., Lele, S. K., Moin, P., Ham, F. E., & Bridges, J. E. (2012). Large-eddy simulation for supersonic rectangular jet noise prediction: Effects of chevrons. In 18th aiaa/ceas aeroacoustics conference (33rd aiaa aeroacoustics conference). doi: 10.2514/6.2012-2212
- Nordström, J., & Svärd, M. (2005). Well-posed boundary conditions for the Navier-Stokes equations. SIAM Journal on Numerical Analysis, 43(3), 1231–1255. doi: 10.1137/040604972
- Ogden, D. E. (2011, 12). Fluid dynamics in explosive volcanic vents and craters. Earth and Planetary Science Letters, 312(3-4), 401–410. doi: 10.1016/j.epsl.2011.10.032
- Ogden, D. E., Glatzmaier, G. A., & Wohletz, K. H. (2008, 4). Effects of vent overpressure on buoyant eruption columns: Implications for plume stability. *Earth and Planetary Science Letters*, 268(3-4), 283–292. doi: 10.1016/j.epsl.2008.01.014
- Ogden, D. E., Wohletz, K. H., Glatzmaier, G. A., & Brodsky, E. E. (2008). Numerical simulations of volcanic jets: Importance of vent overpressure. *Journal of Geophysical Research: Solid Earth*, 113(2), 1–18. doi: 10.1029/2007JB005133
- Poinsot, T. J., & Lelef, S. K. (1992). Boundary conditions for direct simulations of compressible viscous flows. *Journal of Computational Physics*, 101(1), 104–129. doi: 10.1016/0021-9991(92)90046-2
- Richardson, J. P., Waite, G. P., & Palma, J. L. (2014). Varying seismic-acoustic properties of the fluctuating lava lake at Villarrica volcano, Chile. *Journal of Geophysical Research: Solid Earth*, 1–14. doi: 10.1002/2014JB011002 .Received
- Ripepe, M., Marchetti, E., Delle Donne, D., Genco, R., Innocenti, L., Lacanna, G., & Valade, S. (2018). Infrasonic Early Warning System for Explosive Eruptions. *Journal of Geophysical Research: Solid Earth*, 123(11), 9570–9585. doi: 10.1029/2018JB015561
- Rossing, T. D., & Fletcher, N. H. (2004). Principles of Vibration and Sound (Second ed., Vol. 1). Springer. doi: 10.1017/CBO9781107415324.004
- Rowell, C. R., Fee, D., Szuberla, C. A., Arnoult, K., Matoza, R. S., Firstov, P. P., ... Makhmudov, E. (2014). Three-dimensional volcano-acoustic source localization at Karymsky Volcano, Kamchatka, Russia. *Journal of Volcanology and Geothermal Research*, 283, 101–115. doi: 10.1016/J.JVOLGEORES.2014.06.015
- Shariff, K., & Leonard, A. (1992). Vortex Rings. Annu. Rev. Fluid Mech. 1992, 24, 235–279. doi: 10.1146/annurev.fl.24.010192.001315
- Sparks, R., & Wilson, L. (1976). A model for the formation of ignimbrite by gravitational column collapse. *Journal of the Geological Society*, 132(4), 441–451. doi:

10.1144/gsjgs.132.4.0441

959

960

961

963

964

965

966

967

968

970

971

972

973

974

975

976

977

979

980

981

982

983

986

987

988

989

990

991

992

995

996

997

998

999

- Suzuki, Y. J., & Koyaguchi, T. (2012, 4). 3-D numerical simulations of eruption column collapse: Effects of vent size on pressure-balanced jet/plumes. *Journal of Volcanology and Geothermal Research*, 221-222, 1–13. doi: 10.1016/j.jvolgeores .2012.01.013
- Svärd, M., Carpenter, M. H., & Nordström, J. (2007). A stable high-order finite difference scheme for the compressible Navier-Stokes equations, far-field boundary conditions. *Journal of Computational Physics*, 225(1), 1020–1038. doi: 10.1016/j.jcp.2007.01.023
- Vergniolle, S., & Brandeis, G. (1996). Strombolian explosions: 1. A large bubble breaking at the surface of a lava column as a source of sound. *Journal of Geo*physical Research, 101 (B9), 20433. doi: 10.1029/96JB01178
- Vreman, A. W. (2004). An eddy-viscosity subgrid-scale model for turbulent shear flow: Algebraic theory and applications. *Physics of Fluids*, 16(10), 3670–3681. doi: 10.1063/1.1785131
- Watson, L. M., Dunham, E. M., & Johnson, J. B. (2019). Simulation and inversion of harmonic infrasound from open-vent volcanoes using an efficient quasi-1D crater model. Journal of Volcanology and Geothermal Research, 380, 64–79. doi: 10.1016/j.jvolgeores.2019.05.007
- Watson, L. M., Johnson, J. B., Sciotto, M., & Cannata, A. (2020). Changes in crater geometry revealed by inversion of harmonic infrasound observations: 24 December 2018 eruption of Mount Etna, Italy. Geophysical Research Letters.
- Wilson, L., Sparks, R. S. J., Huang, T. C., & Watkins, N. D. (1978). The control of volcanic column heights by eruption energetics and dynamics. *Journal of Geo*physical Research: Solid Earth, 83(B4), 1829–1836. Retrieved from http://dx .doi.org/10.1029/JB083iB04p01829 doi: 10.1029/JB083iB04p01829
- Wilson, L., Sparks, S. J., & Walker, L. (1980). Explosive volcanic eruptions IV: the control of magma properties and conduit geometry on eruption column behaviour. *Geophys. J.R. Astr. Soc.*, 63, 117–148.
- Witsil, A. J., & Johnson, J. B. (2018). Infrasound explosion and coda signal investigated with joint analysis of video at Mount Erebus, Antarctica. *Journal of Volcanology and Geothermal Research*, 357, 306–320. doi: 10.1016/j.jvolgeores .2018.05.002
- Woods, A. W. (1988). The fluid dynamics and thermo dynamics of eruption columns. *Bulletin of Volcanology*, 50, 169–193. doi: 10.1007/BF01079681
- Woulff, G., & McGetchin, T. R. (1976). Acoustic noise from volcanoes Theory and experiment. Geophysical Journal of the Royal Astronomical Society, 45, 601–616. doi: 10.1111/j.1365-246X.1976.tb06913.x
- Yamada, T., Aoyama, H., Nishimura, T., Iguchi, M., & Hendrasto, M. (2017). Volcanic eruption volume flux estimations from very long period infrasound signals. *Geophysical Research Letters*, 44(1), 143–151. doi: 10.1002/2016GL071047